GLOBAL DISTRIBUTION OF ICE CLOUD PARTICLE SHAPE AND ROUGHNESS

FROM PARASOL SATELLITE MEASUREMENTS

A Dissertation

by

BENJAMIN H. COLE

Submitted to the Office of Graduate Studies of
Texas A&M University
in partial fulfillment of the requirements for the degree of

DOCTOR OF PHILOSOPHY

Chair of Committee,	Ping Yang
Committee Members,	George Kattawar
	Sarah Brooks
	R. Lee Panetta
Head of Department,	Ping Yang

August 2013

Major Subject: Atmospheric Sciences

ABSTRACT

The energy balance of the Earth is regulated in part by ice clouds, which both reflect shortwave solar radiation and absorb infrared radiation from the Earth. These clouds appear frequently worldwide, with up to 70% coverage in tropical regions. The microphysics of ice clouds determines their radiative properties, and is important for accurately predicting the role of ice clouds in Earth's energy balance. However, describing the microphysics of ice clouds remains a challenging problem, especially with regard to the shape of ice particles and the degree of ice particle surface roughening. In-situ studies have found evidence for ice surface roughness and have found many complex ice geometries; however, these studies are limited spatially and temporally. An approach which allows large-scale analysis is to retrieve these properties via theoretical modeling using satellite observations of polarized reflectance from ice clouds, since polarized reflectance is sensitive to the shape and roughness of ice particles.

The theoretical model requires the scattering properties of simulated ice particles. These properties are obtained for 10 different ice shapes and 17 different levels of surface roughness. Simulations are performed for 3 different effective ice particle diameters: 30, 60 and 90 μm.

Overall, the retrieved shape is dominated by the compact aggregate of columns. Although the exact composition of shapes varies from month to month, the compact aggregate of columns remains the most commonly retrieved shape.

The retrieved roughness varies from moderately rough at σ = 0.1 to severely rough at σ = 0.5. Retrieved roughness varies more than shape, and smooth surfaced ice is most prominent in January. Tropical regions tend to have ice particles that are more roughened, while the midlatitudes and polar regions tend to have more smooth ice. In almost all cases, roughened ice represents > 60% of the total retrievals.

The asymmetry parameter inferred from the retrieval of ice particle shape and roughness has a mean value near 0.77, with only small differences based on assumed ice effective diameter. The median value of the asymmetry parameter has a nearly constant value of approximately 0.75.

DEDICATION

To my wife Michelle

ACKNOWLEDGEMENTS

I would like to thank my committee chair, Dr. Ping Yang, and my committee members, Dr. Sarah Brooks, Dr. George Kattawar, and Dr. Lee Panetta for their unfailing support through the course of this research.

I would also like to extend my thanks to the wonderful office staff, particularly Barbara and Carria, for their enormous help. Thanks go also to all my ATMO friends and to fellow members of the Dust Devils softball team for the encouragement they gave me and for all the good times we had.

Finally, a special note of gratitude to my family and my wife Michelle. Her patience and unwavering support got me to where I am today.

TABLE OF CONTENTS

LIST OF FIGURES

LIST OF TABLES

CHAPTER I

INTRODUCTION AND BACKGROUND

Ice clouds play an important role in regulating the energy balance of the Earth (Liou 1986), with cloud coverage of up to70% in tropical latitudes (Guignard et al. 2012; Nazaryan et al. 2008). Insufficient knowledge of the shape and degree of surface roughness of ice crystals within ice clouds is a large source of uncertainty in forward light scattering and radiative transfer simulations of ice clouds used in downstream applications such as MODIS (MODerate resolution Imaging Spectroradiometer) satellite ice cloud products. Considerable motivation exists, therefore, to investigate the microphysics of ice clouds in order to reduce the uncertainties in their radiative properties and refine estimates of the impact of ice clouds on the energy balance of the earth.

In order to deliver accurate satellite ice cloud retrieval products, the modeling parameters that go into a retrieval algorithm must accurately represent the cloud being investigated. Changes in the cloud microphysics can have a large impact on radiative properties. Assuming rough ice particles instead of smooth could increase the amount of energy reflected back to space by a factor of two (Baran 2012; Ulanowski et al. 2006). Particle shape can also have a large impact on the radiative properties and can influence the cloud radiative forcing. To reduce these uncertainties and deliver more accurate ice cloud retrieval products to end users, and ultimately better estimates of climate change, we must investigate the microphysics that controls the radiative properties of ice clouds.

1

Previous Studies

The different types of ice particles in ice clouds were first comprehensively described and classified by Magono and Lee (1966). According to this study, the most common habit (shape) is hexagonal, with a column being the most frequently seen of the hexagonal habits. Other habits or variations include rosettes, needles, aggregates, and plates. Ice particle habit geometries can become quite complex, especially larger aggregates of particles. The particle habit depends on many different factors, including the temperature and relative humidity at which the ice formed (Gayet et al. 2011; Korolev et al. 1999). Heymsfield and Miloschevich (2003) showed that the distribution of ice varies from cloud top to base, with more pristine shapes near the cloud top and more complex shapes near cloud base because the particles fall and aggregate together.

Baran (2009) showed images of ice particles from a Cloud Particle Imaging (CPI) probe that are representative of the ice seen in midlatitude and tropical cirrus (ice) clouds. At cloud top, some of the ice seen in the images is small and irregularly shaped, along with a few columns, bullets, and other habits. The abundance of small ice particles is likely due to the shattering of large ice particles on the probe inlet, artificially increasing the amount of small ice seen in the images (Korolev et al. 2011). Compact aggregates and spatial bullet rosettes are also seen and tend to be more common in the midlatitudes (Um; McFarquhar 2007). Some of the observed using the CPI probe also appears to have hollow structures, a feature noted by Magono and Lee (1966) and Baran (2012).

Other types of instruments may be used infer the shape of ice cloud particles,

including the Forward Scattering Spectrometer Probe (FSSP), cloud and aerosol

spectrometer (CAS), polar nephelometer, and the Cloud Integrating Nephelometer

(CIN). See Baumgardner et al. (2011) for an overview of the different measurement

techniques. The CAS instrument uses a focused laser beam to collect the scattering

pattern of the ice particle and infer its shape based on theoretical scattering calculations.

For measurements from July 2002 of a cirrus cloud, Baumgardner et al. (2005) found

that 90% of observations were explained by a model consisting of bullet rosettes, plates,

and columns.

Surface roughness has been observed in laboratory measurements of ice and in

field campaigns (Baran et al. 2011; Ulanowski et al. 2006). Thermodynamic conditions

influence whether an ice particle is roughened and how rough it becomes (Baran et al.

2011), but it is currently unknown what percentage of ice particles in clouds might be

roughened or how rough they are. Nevertheless, observations from the PARASOL

(Polarization and Anisotropy of Reflectances for Atmospheric Sciences coupled with

Observations from a Lidar) satellite indicate a large percentage of ice seen in ice cloudy

scenes has at least some roughness. Any roughness present will affect the radiative

properties of ice clouds by changing the scattering phase function, resulting in less

forward scattering and a lower value of the asymmetry parameter g.

The first study to examine the sensitivity of polarization to the ice habit was

Chefer et al. (1998) who showed that polarized reflectance from an ice cloud is sensitive

to the shape of the ice particles. Subsequent studies tested various ice shapes for their fit

to measured polarized reflectance (Baran; C.-Labonnote 2006, 2007; C.-Labonnote et al. 2001; Cole et al. 2013). Columns were found to be the best fit choice for a single ice shape in the studies by Baran and Labonnote, whereas a mixture of different ice shapes was found to be the best fit in Cole et al. In contrast to previous studies which qualitatively compared simulated polarized reflectance to measured polarized reflectance, this study employs a rigorous retrieval method to quantitatively select the best fit ice shape from the nine ice shapes available in the database and a mixture of ice shapes called the General Habit Mix (Cole et al. 2013).
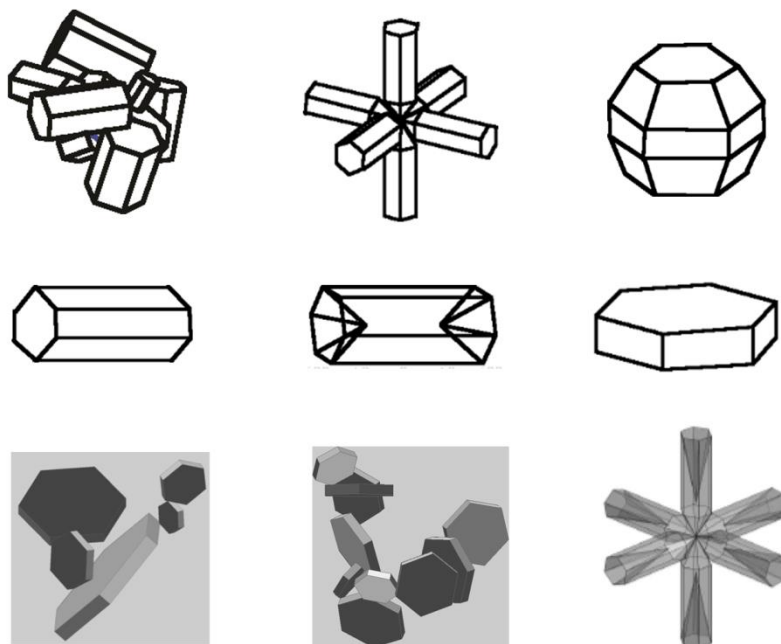
Fig. 1. The nine ice shapes included in the retrieval database.

Upon retrieving the ice particle habit and roughness, the asymmetry parameter g may be inferred from single-scattering calculations. Higher values of g indicate more forward scattering, with 1 being complete forward scattering. Lower values indicate more backscattering.

Ice asymmetry parameters have been inferred from flux measurements and theoretical modeling (Platt et al. 1980; Stephens et al. 1990) with values ranging between 0.7 and 0.85. In situ measurements have yielded values near 0.75 using Cloud Integrating Nephelometer and Polar Nephelometer instruments (Garrett et al. 2005; Gayet et al. 1997; Gerber et al. 2000). In situ measurements generally have limited spatial and temporal resolution, however. Global retrievals of ice particle habit and roughness from PARASOL and subsequent retrieval of the inferred asymmetry parameter can overcome the limited nature of in-situ studies and provide a comprehensive perspective on the asymmetry parameter value in ice clouds.

The aim of the current research to expand upon the knowledge of ice particle shape and roughness currently in the literature by rigorously retrieving ice particle shape and degree of surface roughness using polarized reflectance data from the PARASOL satellite and model output from full-vector adding-doubling radiative transfer simulations. These retrievals will be performed for global data from 1 full day of data selected from four different months of the year. In addition, retrievals for a range of latitudes will be done to examine the sufficiency of a single global ice cloud model in climate simulations, or whether more accurate results might be obtained by assuming different cloud microphysics at different latitudes.

The retrieved shape and roughness from this study will be used to infer the asymmetry parameter and provide estimates of the global mean and median values of g, which is an important parameter in climate models.

Scattering Properties

In order to simulate the reflection of polarized radiation from an ice cloud, the single-scattering properties of the ice particles which compose the cloud must be obtained. These scattering properties are calculated at 0.86 μm for nine different ice shapes plus one ice habit mixture and nine levels of surface roughness from $\sigma = 0$ (no roughness) to $\sigma = 0.8$ (very rough). The 9 habits are droxtals, solid and hollow columns, solid and hollow 3D bullet rosettes, plates, a compact aggregate of columns, and a small and large spatial aggregate of plates, whose geometries are illustrated in Fig. 1. The ice habit mixture is the General Habit Mix (Cole et al. 2013) where the mixture of ice habits for a given size is illustrated in Fig. 2. The method for simulating the surface roughness is to randomly lift and tilt the facet of the ice particle, with the parameter σ describing the level of roughness (Yang; Liou 1998). The calculation is done for ice crystals whose maximum dimension is between 2 and 10,000 μm (Yang et al. 2013). The calculations are done with the ADDA (Amsterdam Discrete Dipole Approximation; (Yurkin; Hoekstra 2011) and the IGOM (Improved Geometric Optics Method; (Yang et al. 2013) methods and the results are stored in a database and then used to calculate the bulk scattering properties. The bulk scattering properties are obtained by averaging over a particle size distribution, instrument response function, solar spectrum, and any habit distribution (none if considering a single shape). Because the scattering phase function

6
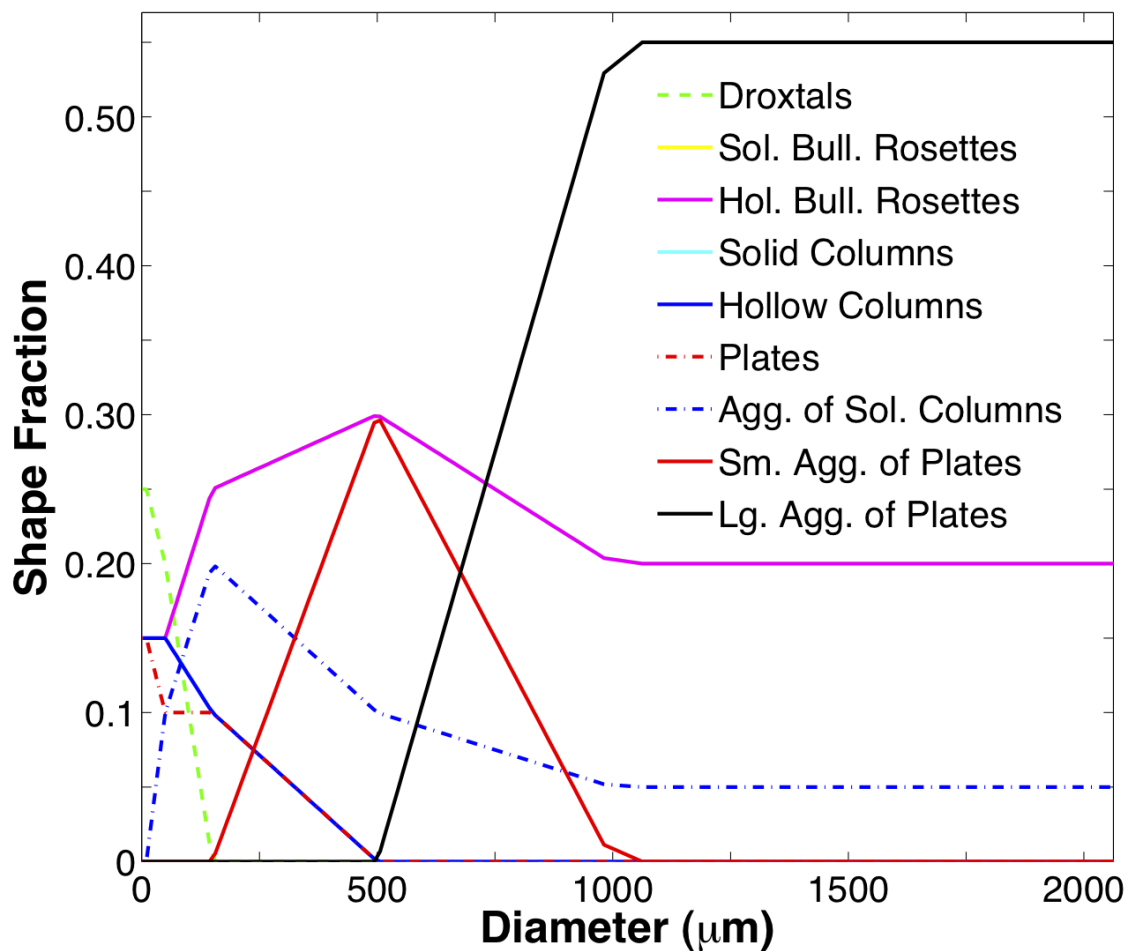
Fig. 2. Fraction of habits used in the General Habit Mix (GHM). Each shape is shown as a function of ice particle maximum diameter.

for ice tends to be strongly peaked in the forward direction, a truncation method must be employed. The method used here is δ-fit (Hu et al. 2000), and after truncation other elements of the phase matrix are normalized. The other scattering parameters of interest including optical thickness and asymmetry parameter are adjusted according to the similarity principle (Joseph et al. 1976).

Radiative Transfer Model

A full vector adding-doubling radiative transfer model based on the code of de Haan et al. (1987) will be used to simulate the top of atmosphere (TOA) Stokes vector for a wide range of input cloud optical depths, viewing geometries, and microphysical parameters. This model has been validated against the tables for Rayleigh scattering given by Natraj et al. (2009) and is accurate to at least 6 decimal places for all viewing geometries.

Retrieval Methodology

Several previous studies have tried to infer ice shape from polarization measurements. Labonnote (2001) used polarized reflectance with a variety of ice models to try to find a best match to observations. Baran and Labonnote (2006) took the same approach for a greater variety of ice models. In all cases models which had some kind of inclusion or roughening matched polarized reflectance the best. Van Diedenhoven et al. (2012) presented a method to infer the ice asymmetry parameter by using polarized reflectance measurements from the RSP (Research Scanning Polarimeter) aircraft instrument. The authors used a lookup table of polarized reflectance built using columns

and plates with varying aspect ratios and roughness and minimized differences between the observed and lookup table values.

The approach in this study is similar to that of van Diedenhoven et al. (2012). Using the adding-doubling radiative transfer model, simulations of polarized reflectance are performed for 17 values of surface roughness from $\sigma = 0$ to $\sigma = 0.8$ in .05 increments. Nine ice shapes and a mixture of shapes are included. Cloud optical thickness must be considered for optical thickness below 5, because polarized reflectance saturates at that optical thickness but depends on the thickness below a value of 5 (van Diedenhoven et al. 2013). Values from 1.0 to 5 for optical thickness are used in this study with an increment of 0.5.

In all, ten different habits, 17 roughness values, and nine values for optical thickness are considered, making 1530 distinct combinations. When running a simulation for any one of the combinations, many different viewing geometries must be used to reproduce the full range of observations from PARASOL. Solar zenith angles from 0 (nadir) to 80 degrees in 4 degree increments are used, along with viewing zenith from 0 to 75 degrees in 4 degree increments and relative azimuth from 0-180 degrees in 4 degree increments. This covers the viewing geometries typically seen from PARASOL (Breon 2009).

The quantity to be minimized in the retrieval algorithm is the relative root mean square error (van Diedenhoven et al. 2012) defined as:

$$\text{RRMSE} = \sqrt{\frac{\Sigma_{j=1}^{J}\left[1 - \frac{L_{nmp(sim)}(\Theta_j, h, \sigma)}{L_{nmp(PAR)}(\Theta_j)}\right]^2}{J}}. \tag{1}$$

9

Here h is habit, σ is level of roughness, and θ is scattering angle. Lnmp is the normalized, modified, polarized reflectance (C.-Labonnote et al. 2001):

$$L_{nmp}(\theta_v, \varphi_v, \theta_s, \varphi_s) = \frac{\pi L_p}{E_s} \frac{\cos\theta_s + \cos\theta_v}{\cos\theta_s}, \qquad (2)$$

Es is the extraterrestrial solar irradiance, and L_p is the polarized radiance:

$$L_p = \pm\sqrt{Q^2 + U^2}. \qquad (3)$$

When a pixel is retrieved, the first step is to read out the viewing geometries from the available viewing directions which can be up to 16. For each geometry, the polarized reflectance is calculated for every possible combination of habit and roughness in the lookup table. In order to select habit and roughness from the appropriate optical thickness, the optical thickness in the PARASOL Level-2 data file is read out and if the value is < 5 the closest match to the PARASOL specified value that exists in the lookup table will be used. If the PARASOL optical thickness is > 5, an optical thickness of 5 will be used since polarization will be saturated and no longer depends on the optical thickness.

When the polarized reflectance for all possible combinations of habit and roughness have been calculated from results in the lookup table for all viewing geometries in the pixel, the RRMSE is calculated for each of the combinations and then the habit and roughness associated with the smallest value of the RRMSE are considered the retrieved values. This procedure is repeated for all pixels in the PARASOL dataset to give a global dataset of retrieved habit and roughness.

PARASOL Satellite

   The PARASOL satellite is a French microsatellite launched in 2004 to become part of the A-Train satellite constellation of Earth-observing satellites. It is in a nearly circular polar orbit at an altitude of 705 km (Fougnie et al. 2007). It has 9 channels, 3 of which have polarization capability. For this study, one full day of data from four separate months will be used. The four dates are 1 January 2007, 1 April 2007, 1 August 2007, and 15 October 2007. These 4 days of data will give an indication of the whether there is variation throughout the year in global polarized reflectance observed by PARASOL.

   The 0.86 μm channel is used in this study and only data over the ocean will be considered since the ocean surface is dark and nearly non-polarizing at this wavelength. About 14 orbits are represented in each day of data, providing near global coverage. Each pixel from the Level 2 cloud product data considered is approximately 18 x 18 km and the parameters available are reflectance and polarized, normalized radiance. Pixels will be chosen for use in the study if the Level-2 cloud product indicates that the pixel is ice phase, is over the ocean, has 100% cloud cover, and has at least 7 viewing geometries available covering a scattering angle range of at least 50 degrees. This ensures that features in the scattering pattern over a large range of angles will be resolved in the retrieval method.

CHAPTER II

POLARIZATION

The Electric Field

The vector nature of electromagnetic waves must be considered since this study involves polarization, which is the direction of the electric field. The vector radiative transfer equation is used in this case since it fully considers the vector nature of the incident radiation. In addition, the inclusion of polarization comes with the added benefit of more exact computation of radiances, as Adams and Kattawar (1993) showed. The intensity is not fully independent of the polarization state so without polarization small errors are introduced.

Electromagnetic radiation is a transverse wave, meaning that the electric and magnetic fields oscillate in a direction perpendicular to the propagation direction (Jackson 1998). The direction of the electric field vector defines the polarization state of the electromagnetic wave.

Since it is a vector, an electromagnetic wave can be decomposed into the sum of two components. First, a meridian plane is defined as the plane containing the direction of propagation and the zenith direction (+z), then the electric field is written as the sum of a component parallel to the meridian plane and a component perpendicular to the meridian plane. These two components are also perpendicular to the direction of propagation. Fig. 3 provides an illustration of the described geometry.
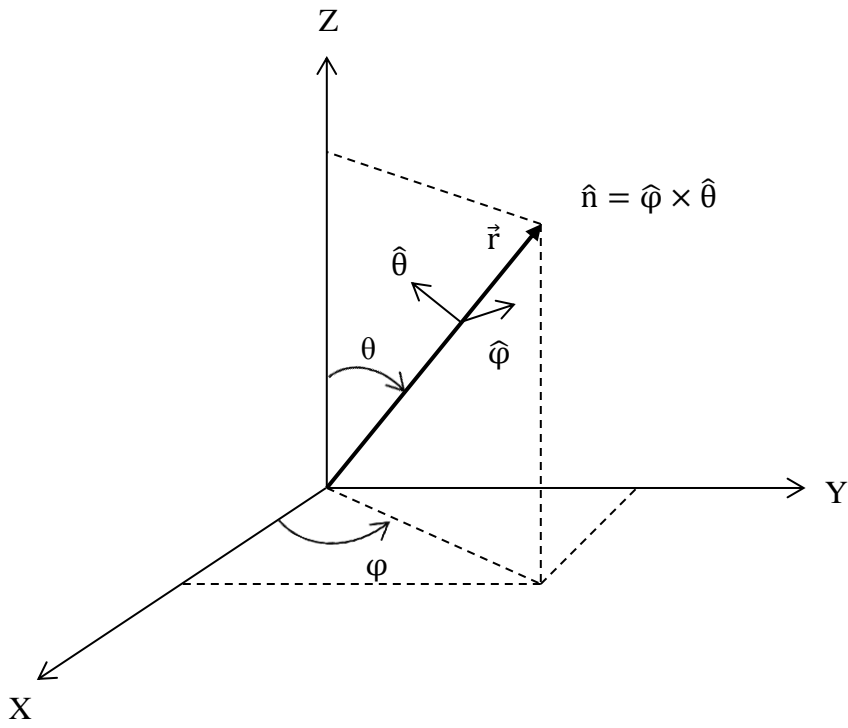
Fig. 3. Coordinate system for the electric field. $\hat{\theta}$ denotes the

direction of the meridian plane.

This radiation can be described as a plane wave with equation:

$$\vec{E} = \vec{E}_{\parallel} + \vec{E}_{\perp} = \left[E_{\parallel}\hat{\theta} + E_{\perp}\hat{\varphi}\right]\exp[-i(k\hat{n}\cdot\vec{r} - \omega t)]\,. \qquad (4)$$

The direction of propagation is $\hat{n}$, contained in the meridian plane, seen in Fig. 3. The vector $\vec{r}$ connects the origin to the observation point, ω is the angular frequency, k is the wavenumber, and the unit vectors $\hat{\theta}$ and $\hat{\varphi}$ are perpendicular to the propagation direction. It follows then that $\hat{\varphi} \times \hat{\theta} = \hat{n}$.

Note that the terms $E_{\parallel}$ and $E_{\perp}$ are complex amplitudes with an amplitude and a phase, meaning that the previous result can be expressed as:

$$\vec{E} = \left[a_{\parallel}\exp(-i\delta_{\parallel})\,\hat{\theta} + a_{\perp}\exp(-i\delta_{\perp})\,\hat{\varphi}\right]\exp[-i(k\hat{n}\cdot\vec{r} - \omega t)]\,. \qquad (5)$$

Chandrasekhar (1947) remarked that for unpolarized electromagnetic radiation, the complex amplitudes are not stable in the time or space domain and are not mathematically related. If relationships do exist among these components, the beam is polarized to some degree.

Polarization in Detail

Polarization described in the most general way is of the elliptical variety, where the electric field vector traces an ellipse when viewed with the beam traveling toward the observer. Fig. 4 illustrates the concept. For varying amplitudes and phase differences of the electric field components $\delta = \delta_{\parallel} - \delta_{\perp}$, linear and circular polarization may also be obtained. Table 1 provides an overview of possible polarization states. The total electric field for each case can be retrieved by inserting the values from Table 1 into Eq. (5).

14

Table 1. Range of possible polarization states. The amplitude and phase differences for each polarization are shown as well.

State of polarization	Amplitude	Phase difference $\delta = \delta_{\parallel} - \delta_{\perp}$
Elliptical	$a_{\parallel} \neq a_{\perp}$	$\neq 0$ $\neq \pm 2m\pi \qquad m = 1,\infty$
Linear	$a_{\parallel} \neq a_{\perp}$ or $\quad a_{\parallel} = a_{\perp}$	$= 0$ $= \pm 2m\pi \qquad m = 1,\infty$
Circular	$a_{\parallel} = a_{\perp}$	$= \pm(2m+1)\frac{\pi}{2} \quad m = 0,\infty$

Natural light, or solar radiation, is unpolarized (Hecht 2002) and consists of rapid variations in the polarization state, meaning the time-averaged polarization is near zero. Referring back to **Fig. 4**, the polarization ellipse of the beam rapidly changes shape and orientation in time. It is important to note that so-called unpolarized radiation is not polarization-free, simply that the random fluctuations of polarization cancel out, leaving a time-averaged polarization of zero. This study will be concerned with randomly polarized radiation from the sun. To incorporate randomly polarized radiation into the radiative transfer equation, a method for mathematically representing the polarization state of a beam of radiation in the equation must be introduced. Chandrasekhar (1960) adopted the Stokes parameters, derived in 1852 by Sir George Stokes (Stokes 1975), for this purpose in his treatment of polarization in the radiative transfer equation, and this is the approach that the current study will adopt as well.
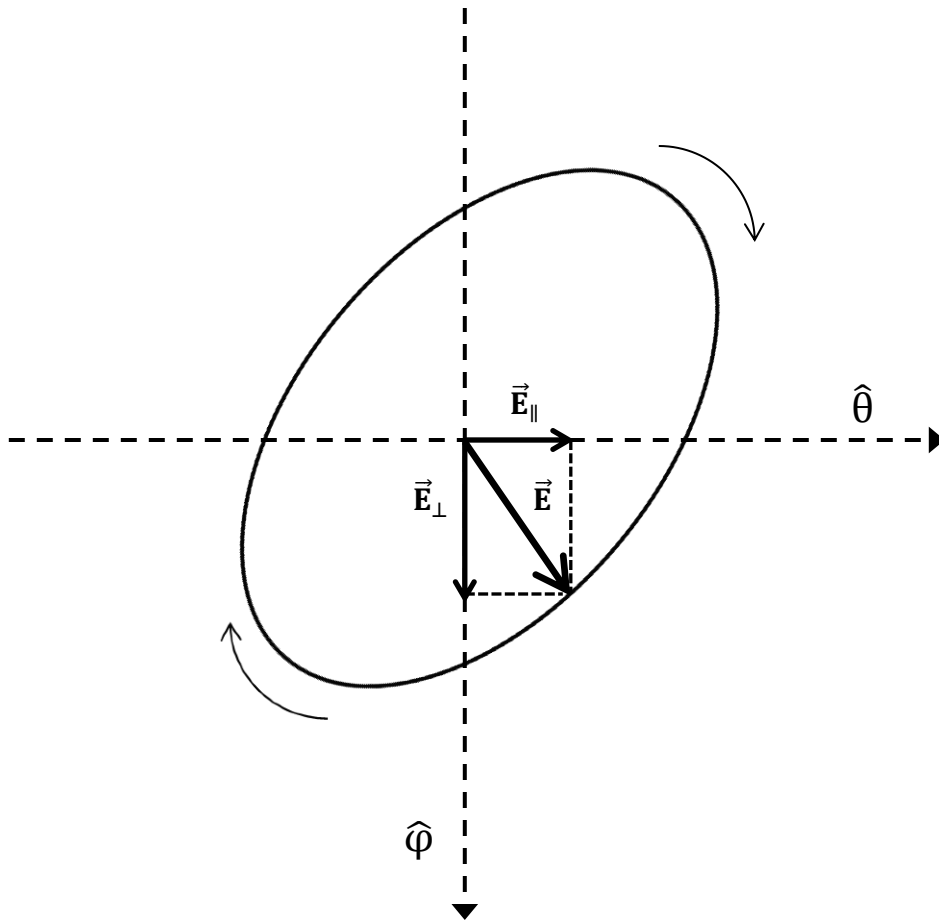
Fig. 4. Elliptically polarized beam. The propagation direction is given by the right-hand rule (out of the page) and the total vector traces an ellipse in the clockwise direction through time.

Complete Description of a Beam of Light

In order to completely describe electromagnetic radiation, four things need to be specified: the intensity, plane and degree of polarization, and ellipticity (Chandrasekhar 1960). Chandrasekhar says that it would be quite difficult to include in the radiative transfer equation "an intensity, a ratio, an angle, and a pure number in any symmetrical way" (Chandrasekhar 1960). However, the Stokes parameters contain information about all four of these parameters, and can be included in the radiative transfer equation instead of the scalar quantity I, which does not include any information about polarization.

The Stokes vector is a four-element column vector composed of I, Q, U, and V, the four Stokes parameters. These are quantities which can be measured experimentally, where I is the intensity, Q is the linear polarization either parallel or perpendicular to a chosen axis, U is the linear polarization at $+45°$ or $-45°$ to that axis, and V is the circular polarization. Many different but equivalent ways exist to define the Stokes parameters; three ways will be detailed here.

Following van de Hulst (1957), the Stokes parameters can be expressed in the following way (c.f. Eq. (4)):

$$I = E_\parallel E_\parallel^* + E_\perp E_\perp^*$$

$$Q = E_\parallel E_\parallel^* - E_\perp E_\perp^*$$

$$U = E_\parallel E_\perp^* + E_\perp E_\parallel^*$$

$$V = i(E_\parallel E_\perp^* - E_\perp E_\parallel^*) \,, \tag{6}$$

where the asterisk denotes a complex conjugate. A constant term ($k/2\omega\mu_0$) (Bohren;

Huffman 1983) has been left out of each of the Stokes parameters because most of the

time the relative Stokes parameters are examined instead of the absolute Stokes vector.

The constant gives the Stokes vector components the units of energy per area per time,

or irradiance.

Another way to write the Stokes parameters involves the equation for a plane

wave with amplitude a and phase δ for each component (c.f. Eq. (5)). Using this

formalism, the Stokes parameters can be written:

$$I = a_\parallel^2 + a_\perp^2$$

$$Q = a_\parallel^2 - a_\perp^2$$

$$U = 2a_\parallel a_\perp \cos\delta$$

$$V = 2a_\parallel a_\perp \sin\delta \ . \tag{7}$$

As before, δ is the phase difference $\delta_\parallel - \delta_\perp$ of the components.

The third way to represent the Stokes parameters can be done in an intuitive way

from the geometry involved with a polarization ellipse. Considering a polarization

ellipse as in Fig. 5, the electric field vector can be expressed as follows:

$$\vec{E} = a\hat{p}\cos\beta\sin(\omega t - k\hat{n}\cdot\vec{r} + \alpha) + a\hat{q}\sin\beta\cos(\omega t - k\hat{n}\cdot\vec{r} + \alpha) \ . \tag{8}$$

The unit vectors $\hat{p}$ and $\hat{q}$ are unit vectors along the long and short axes, respectively, and

α is an arbitrary phase angle.
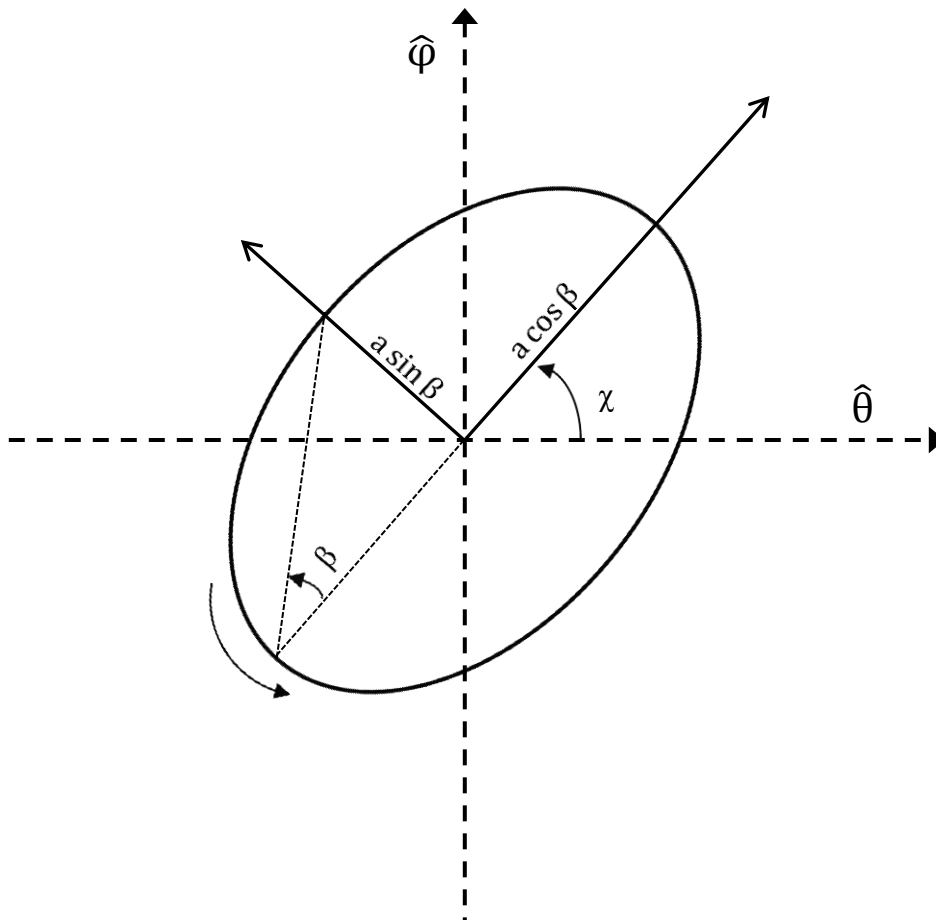
Fig. 5. Polarization ellipse. This shows angles involved in determining the polarization state. It is an elliptically polarized beam rotating in the counter-clockwise direction and is right-handed, with the direction of propagation into the page ($\widehat{\boldsymbol{\varphi}} \times \widehat{\boldsymbol{\theta}}$).

The Stokes parameters can then be rewritten in the following form:

$$I = a^2$$

$$Q = a^2 \cos 2\beta \cos 2\chi$$

$$U = a^2 \cos 2\beta \sin 2\chi$$

$$V = a^2 \sin 2\beta \quad . \tag{9}$$

The quantity $\tan \beta$ is a measure of the ellipticity, where 0 is for linear polarization, -1 for left-circular polarization, and +1 for right-circular polarization.

There are two different conventions for right handed and left handed circular polarization in the literature; see van de Hulst (1957), Chandrasekhar (1960), Hovenier (2004), and others for one convention where the direction of rotation of the electric field vector is observed looking down the beam as it propagates away from the observer. In this study the convention of Bohren and Huffman (1983) will be followed, where the direction of rotation viewed as a beam of radiation propagates toward an observer. It follows that right-circular polarized light will appear to rotate in the clockwise direction as it moves toward the observer. The conventions in Bohren and Huffman will also be followed for linearly polarized radiation.

Fig. 6 summarizes the different states of polarization and their Stokes vectors.

All the quantities of the Stokes vector are *time averages*, because when measuring the Stokes vector components, superpositions of many different incident waves are actually being measured over a very short time period. In other words, the amplitudes and phases of the electric field components which were assumed previously

to be invariant in time are in fact varying on a very short time scale. This means that in general light is partially polarized, and the following relation applies:

$$I^2 \geq Q^2 + U^2 + V^2 \,. \tag{10}$$

If the amplitudes and phases are correlated in time, then the light is said to be fully polarized and the previous inequality becomes an equality.

The degree of polarization is defined in the following way:

$$DOP = \frac{\sqrt{Q^2+U^2+V^2}}{I} \tag{11}$$

and the degree of linear polarization is:

$$DLP = \frac{\pm\sqrt{Q^2+U^2}}{I} \,. \tag{12}$$

The degree of linear polarization is a quantity useful in satellite remote sensing of polarized reflectance used in this study.

Because the Stokes vector completely describes a beam of light, a corollary which can be found is the principle of optical equivalence which states that that if two beams have the same Stokes parameters, there is no experimental way to distinguish them, even if they were formed by interaction with different media (van de Hulst 1957). The significance of this statement is that the Stokes parameters are the complete and only set of quantities needed to define experimentally the intensity and state of polarization of a beam of radiation. There can be further theoretical differences, but these do not correspond to anything physically measurable.

$0°$	$90°$	$+45°$
$\longleftrightarrow$ $\begin{bmatrix} 1 \\ 1 \\ 0 \\ 0 \end{bmatrix}$	$\updownarrow$ $\begin{bmatrix} 1 \\ -1 \\ 0 \\ 0 \end{bmatrix}$	$\nwarrow\!\!\!\searrow$ $\begin{bmatrix} 1 \\ 0 \\ 1 \\ 0 \end{bmatrix}$
-45°	**Right**	**Left**
$\nearrow\!\!\!\swarrow$ $\begin{bmatrix} 1 \\ 0 \\ -1 \\ 0 \end{bmatrix}$	$\begin{bmatrix} 1 \\ 0 \\ 0 \\ 1 \end{bmatrix}$	$\begin{bmatrix} 1 \\ 0 \\ 0 \\ -1 \end{bmatrix}$

Fig. 6. Stokes parameters of polarized light. Circular polarization handedness is determined looking toward a beam of radiation propagating in the direction of the observer.

In the case that there is no phase relationship among multiple beams of radiation, the Stokes parameters of the beams are additive. This concept is crucial where multiple scattering is considered because there can be contributions of many beams to the outgoing measured beam in a certain solid angle. A beam of radiation incident on the surface of a medium has a certain Stokes vector, and after interaction with the medium its Stokes vector is transformed in a new, scattered Stokes vector. The change in the Stokes vector from interaction with the medium is described mathematically by a 16-element 4x4 matrix called a transformation matrix F by van de Hulst (1957), and when normalized, called the scattering phase matrix or Mueller matrix M (Mueller 1948). The interaction takes the following form:

22

$$\begin{bmatrix} I_s \\ Q_s \\ U_s \\ V_s \end{bmatrix} = M(\mu, \mu', \varphi - \varphi') \begin{bmatrix} I_0 \\ Q_0 \\ U_0 \\ V_0 \end{bmatrix}, \qquad (13)$$

where the subscript s is for the scattered Stokes vector. The Mueller matrix contains all information about the medium at the specified wavelength and viewing geometry. All 16 elements of the Mueller matrix may be retrieved in an experiment with 49 intensity measurements (Hielscher et al. 1997), but in many cases some of the elements are not independent of each other or could be zero if there are symmetries involved, as in the case of spheres and other geometries.

The adding-doubling radiative transfer model used in this study can be used to derive the Mueller matrix of a target medium by considering four different incident polarization states: a Stokes vector of [1,0,0,0], corresponding to unpolarized light; a Stokes vector of [1,1,0,0], corresponding to light polarized at $0°$; a Stokes vector of [1,0,1,0], corresponding to light polarized at $+45°$; and a Stokes vector of [1,0,0,1], corresponding to right-circularly polarized light. However, since the scope of this study involves only scattering of unpolarized solar radiation from ice clouds, only the first column of the Mueller matrix can be compared with measurements from the PARASOL satellite.

The Full Vector Form of the Radiative Transfer Equation

Now nearly all the ingredients needed to describe polarization in the vector radiative transfer equation have been assembled. What is commonly called the phase function in the scalar version of the radiative transfer equation is a 4x4 scattering matrix in the vector radiative transfer equation, which is the product of the single scattering

Mueller matrix and two rotation matrices. These rotation matrices are needed because the Stokes parameters are defined in the meridian plane, so the matrices first rotate the incident Stokes vector into the scattering plane (a plane containing the incident and scattered directions) where the Mueller matrix acts on it, then rotate the scattered Stokes vector back to the meridian plane of the scattered beam. The scattering process and rotations can be written as:

$$\mathbf{I}_s = \mathbf{R}(\pi - \alpha_2)\mathbf{M}(\Theta)\mathbf{R}(-\alpha_1)\mathbf{I}_0 \ . \tag{14}$$

The right hand side of the equation has terms that must be applied from right to left, meaning the angle α_1 is the rotation angle from the meridian plane into the scattering plane, and the angle α_2 is the rotation angle from the scattering plane into the meridian plane of the scattered Stokes vector.

The first three terms on the right hand side are the phase matrix $\mathbf{Z}$:

$$\mathbf{Z}(\theta, \varphi, \theta', \varphi') = \mathbf{R}(\pi - \alpha_2)\mathbf{M}(\Theta)\mathbf{R}(-\alpha_1) \ . \tag{15}$$

$\mathbf{M}(\Theta)$ is the 16-element single scattering Mueller matrix:

$$\mathbf{M}(\Theta) = \begin{bmatrix} M_{11} & M_{12} & M_{13} & M_{14} \\ M_{21} & M_{22} & M_{23} & M_{24} \\ M_{31} & M_{32} & M_{33} & M_{34} \\ M_{41} & M_{42} & M_{43} & M_{44} \end{bmatrix} , \tag{16}$$

and the rotation matrix $\mathbf{R}$ is the following, defined by van de Hulst (1957):

$$\mathbf{R}(\alpha) = \begin{bmatrix} 1 & 0 & 0 & 0 \\ 0 & \cos 2\alpha & \sin 2\alpha & 0 \\ 0 & -\sin 2\alpha & \cos 2\alpha & 0 \\ 0 & 0 & 0 & 1 \end{bmatrix} . \tag{17}$$

Before fully traversing a medium, the radiation may be scattered multiple times, leading to many interactions of the type in Eq. (14). The final Stokes vector after

considering the repeated interactions is the matrix multiplication of the n number of interactions:

$$\mathbf{I_s} = (\mathbf{Z_n Z_{n-1} ... Z_1})\mathbf{I_0} \ . \tag{18}$$

The product of the n number of phase matrices $\mathbf{Z}$ is called the effective Mueller matrix (Tynes et al. 2001). Normally the reduced effective Mueller matrix is examined instead of the effective Mueller matrix in order to see polarization effects. To get the reduced effective Mueller matrix, each element of the effective Mueller matrix is divided by the M_{11} element.

The vector radiative transfer equation including the Stokes vector is defined as the following:

$$\mu \frac{d\mathbf{I}(\tau,\mu,\varphi)}{d\tau} = \mathbf{I}(\tau,\mu,\varphi) - \mathbf{J}(\tau,\mu,\varphi) \ . \tag{19}$$

The source function is given by:

$$\mathbf{J}(\tau,\mu,\varphi) = \frac{\widetilde{\omega}_0}{4\pi} \int_0^{2\pi} \int_{-1}^{1} \mathbf{Z}(\mu,\mu',\varphi-\varphi')\mathbf{I}(\tau,\mu',\varphi')d\mu'\varphi' \ . \tag{20}$$

$\mathbf{Z}$ is the reduced effective Mueller matrix for multiple scattering, and $\widetilde{\omega}_0$ is the single scattering albedo, which is the ratio of scattered to absorbed radiation. Eq. (20) gives the full description of the transfer of electromagnetic radiation through a medium, including the effects of polarization.

CHAPTER III

ICE PARTICLE SCATTERING PROPERTIES

The adding-doubling radiative transfer model used in this study requires as input

the scattering properties describing the medium through which the radiation will

propagate, which in this case is an ice cloud. The single scattering properties of different

ice shapes and roughnesses are calculated by various methods including IGOM and

ADDA, and then a size distribution is applied, meaning that the scattering properties are

weighted for the fraction of ice particles in each size bin of the distribution. If a

collection of different ice shapes is used instead of one shape, a habit (shape) distribution

is used. Finally, the spectral response function (SRF) of the satellite sensor must be

taken into account in the integration process. The end result is a set of average bulk

scattering properties describing how radiation will scatter from the simulated ice cloud.

The PARASOL 0.865 μm (central wavelength) channel will be used in this study.

The IGOM Method

Scattering problems involving very small particles are easier to solve by either

exact methods or approximate methods, but there is currently no exact method to

calculate the scattering from a large particle with potentially complicated geometry like

an ice crystal. Approximate methods can be employed, however. The geometric optics

method is one of these approximate methods and can be used if the wavelength of the

incident light is much smaller than the size of the ice particle (meaning the size

parameter is large). In the current study the wavelength considered is 865 nm. Since the

smallest ice crystals considered are at minimum one order of magnitude larger than the wavelength, the geometric optics method may safely be employed.

In geometric optics, a beam of radiation is considered a plane wave, with the wave front composed of many small rays propagating perpendicular to the wave front. In order for the calculations to be valid the width between each ray must be smaller than the size of the ice particle, but larger than the wavelength of the incident light. If this condition is not satisfied then diffraction due to phase interference breaks down the assumption of a ray as a plane wave (Ditchburn 1991). In the geometric optics method, four laws govern the interaction of radiation with matter: reflection, refraction, straight-line propagation, and the principle of reversibility. The last law embodies the principle that if a ray is reversed, it will travel in the opposite direction but take the exact same past as it took to get to its current point. When a ray reaches an ice surface it can be either reflected or refracted with the new direction and polarization depending on the properties of the ice particle considered and the incident direction of the ray. Even when rays are spaced far apart they can interact with each other and changes in phase can occur, an effect incorporated into the geometric optics method (Yang; Liou 1996).

One phenomenon that standard geometric optics cannot account for is diffraction, which causes a large increase in the amount of scattered radiation in the forward direction. Large particles in particular will cause more scattering in the forward direction from diffraction, which visually would be radiation getting bent around the particle and focused into the forward direction.
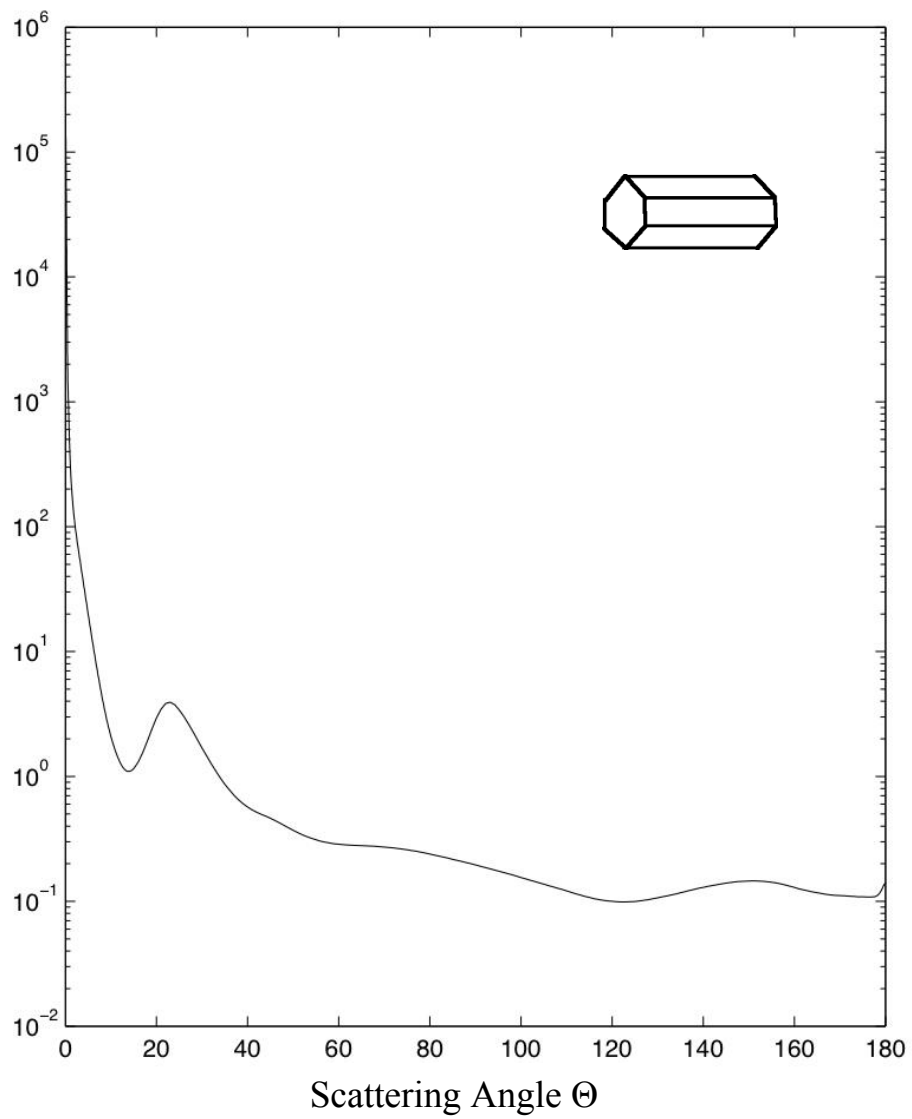
Fig. 7. Phase function of a solid hexagonal column crystal. The effective diameter is 90 μm.

Fig. 7 shows the distribution of scattered radiation for a hexagonal ice crystal as a function of scattering angle. The forward direction is 0 degrees and the backward direction is 180 degrees. This distribution is commonly called the phase function, and as seen here the forward peak is many orders of magnitude larger than the scattered intensity at other angles due to the diffraction effect. Later version of the geometric optics method such as IGOM do include a treatment of diffraction in the calculation of single scattering properties.

Yang and Liou (1997) used a ray-by-ray integration algorithm to obtain the far field solution for the scattered electric field by integrating the near field electric field solution inside the particle from the geometric optics method. In this way the full scattered field and the extinction and absorption cross sections can be obtained, along with the single scattering albedo. This combined algorithm was named the Improved Geometric Optics Method. Yang and Liou compared their code with a reference finite-difference time domain (FDTD) result for size parameters down to 20 and found good agreement (Yang; Liou 1997).

Bi et al. (Bi et al. 2009) made significant improvements to the IGOM method, specifically for the treatment of rays that pass through two opposing faces of an ice crystal in the forward direction. Improvements were made for the mapping of the near field to the far field in the ray-by-ray integration method with regard to polarized ray spreading and the δ-transmission term for forward scattering through these faces was dropped. The calculation of the phase function at backscattering angles was also made more accurate (Bi et al. 2009).

Based on observations showing that ice particles can have rough surfaces, a way to incorporate surface roughness was also added to the model. Two different ways to incorporate surface roughness were compared in Yang et al. (2008). The first was a rigorous ray-tracing method where each external ray reflected from a roughness facet or emerging internal ray from a roughness facet was tracked to see if it interacted with another roughness facet. There could be many interactions among roughness facets before a ray finally leaves the particle, and all of these interactions take large amounts of computational time to calculate. Another approach which avoids the issue of repeated interactions was also investigated. In this second method the normal to the surface for each reflection or refraction event was changed and replaced with a random angle selected from a distribution. In this way multiple reflections and refractions are avoided because the surface for each individual event is just a flat facet. The two methods produced comparable results, leading the second method being chosen for use in calculations (Yang et al. 2008). The spatial orientations of the rough surfaces come from a Gaussian distribution with a parameter σ that quantifies the level of roughness. In the present study, 17 levels of surface roughness were used from $\sigma = 0$ (smooth) to $\sigma = 0.8$ with increments of 0.05. The roughness parameter σ cannot be related to a measurable length scale because the roughness is not rigorously represented in the model, but the variations in the slopes of the ice surface are still large enough to have an effect on the incident beam (Yang et al. 2008). The effect of surface roughness is to smooth out the phase function and make it almost featureless, removing all halo peaks for a value of $\sigma = 0.5$ and almost all evidence of halo peaks for $\sigma = 0.05$. Sharp halo peaks are not usually

seen in remote sensing measurements of scattering and surface roughness could be the

reason why (Baum et al. 2010).

The ADDA Method

The Amsterdam Discrete Dipole Approximation (Yurkin; Hoekstra 2011) is a

method to calculate the scattering properties of arbitrarily shaped particles by the use of

small dipoles that are stacked together until a shape approximating the shape of interest

is found. Complex shapes can be simulated in this way and then Maxwell's equations

can be solved directly to obtain the scattered radiation field. This method is

computationally most efficient for small particle sizes; in this study, the ADDA method

is used for size parameters less than 20, while the IGOM method was used for size

parameters larger than 20.

Scattering Phase Matrix

The scattering phase matrix describes completely how radiation will scattering

from some ice particle of a certain shape and size. To understand how it is calculated,

first consider an arbitrary incident ray on an ice particle. This incident ray will have an

amplitude and phase with respect to an initial reference plane, while the scattered ray

will have another amplitude and phase with respect to the scattering plane.

The mathematics describing the interaction are given by van de Hulst (1957), in the form

of four complex functions:

$$S = \begin{bmatrix} S_2 & S_3 \\ S_4 & S_1 \end{bmatrix}. \tag{21}$$

These functions mathematically relate the transformation of the electric field from one

state to another. Most of the time the far field solution is the one used in practical

applications, where kr >> 1 (Liou 2002). The scattered electric field is then (van de Hulst

1957):

$$\begin{bmatrix} E_\parallel^s \\ E_\perp^s \end{bmatrix} = \begin{bmatrix} S_2 & S_3 \\ S_4 & S_1 \end{bmatrix} \frac{\exp(-ikr+ikz)}{ikr} \begin{bmatrix} E_\parallel^0 \\ E_\perp^0 \end{bmatrix}. \tag{22}$$

The four S parameters depend on the incident and outgoing directions θ and the

orientation of the ice particle with respect to the incoming beam. The 16-element

transformation matrix for the Stokes vector is a function of these amplitude functions S.

This transformation matrix (van de Hulst 1957), when normalized, is referred to as the

scattering phase matrix (Liou 2002). The scattering phase matrix and the single

scattering Mueller matrix are proportional to each other.

Using these results, the scattered Stokes parameters can be expressed as:

$$\begin{bmatrix} I_s \\ Q_s \\ U_s \\ V_s \end{bmatrix} = \frac{\sigma_s \mathbf{P}}{4\pi r^2} \begin{bmatrix} I_0 \\ Q_0 \\ U_0 \\ V_0 \end{bmatrix}, \tag{23}$$

where $\mathbf{P}$ is the scattering phase matrix, and σ_s is the scattering cross section,

representing the fraction of energy scattered out of the beam and lost.

The scattering cross section is calculated with a straightforward formula given here,

which integrates the intensity over all scattering angles:

$$\sigma_s = \frac{1}{k^2} \int_0^{2\pi} \int_0^\pi \left(E_\parallel^s E_\parallel^{s*} + E_\perp^s E_\perp^{s*} \right) \sin\theta \, d\theta d\varphi \,. \tag{24}$$

The scattering phase matrix is given by:

$$\mathbf{P}(\Theta, \alpha, \beta) = \begin{bmatrix} P_{11} & P_{12} & P_{13} & P_{14} \\ P_{21} & P_{22} & P_{23} & P_{24} \\ P_{31} & P_{32} & P_{33} & P_{34} \\ P_{41} & P_{42} & P_{43} & P_{44} \end{bmatrix}. \tag{25}$$

It can be seen from Eq. (25) that $\mathbf{P}$ depends on the incident and outgoing directions and the angle at which the incident radiation hits the ice crystal, which is found by using the angles α and β.

Several concepts are used by van de Hulst (1957) to reduce the number of non-zero phase matrix elements. If a random sample of ice particles of the same size is taken in which the particles are randomly oriented in space, many symmetries can be found which will cancel terms. To cancel the terms depending on ice particle orientation (since they are randomly oriented), an integration over all orientations can be performed:

$$\mathbf{P}(\Theta) = \frac{1}{2\pi\sigma_s} \int_0^{2\pi} \int_0^{\frac{\pi}{2}} \mathbf{P}(\Theta, \alpha, \beta)\sigma_s(\alpha, \beta) \sin \alpha \, d\alpha \, d\beta \, . \tag{26}$$

Then doing the same thing for the scattering cross section yields:

$$\sigma_s = \frac{1}{2\pi} \int_0^{2\pi} \int_0^{\pi} \sigma_s(\alpha, \beta) \sin \alpha \, d\alpha \, d\beta \, . \tag{27}$$

According to van de Hulst (1957), for a certain position of a particle there are three other positions where the scattering phase matrix is the same as the first position. The so-called reciprocal position is the first, found by rotation around the line that bisects the supplement to the scattering angle (called the "bisectrix" by van de Hulst (1957)). Second is the mirror image with respect to the bisectrix plane, with the last being the mirror image with respect to the scattering plane. If the assumption is made that the collection of ice particles has an equal number of all of the possible positions, then the scattering phase matrix simplifies in the following way:

$$\mathbf{P}(\Theta) = \begin{bmatrix} P_{11} & P_{12} & 0 & 0 \\ P_{12} & P_{22} & 0 & 0 \\ 0 & 0 & P_{33} & -P_{43} \\ 0 & 0 & P_{43} & P_{44} \end{bmatrix} . \tag{28}$$

33

Eq. (28) is the form of the scattering phase matrix which IGOM will produce for each size and shape of ice crystal.

Scattering Properties to Describe a Bulk Volume

Once the single scattering properties describing scattering from a single particle have been obtained the next step is to find the scattering properties that describe a volume containing many ice particles. This is done by incorporating size and habit distributions as well as the spectral response function of the PARASOL satellite sensor and the solar flux at the sensor wavelengths. The adding-doubling model takes the average scattering properties as input, so the single scattering properties of different sizes and shapes are averaged together to produce a consistent set of scattering properties that describes a volume for use in the radiative transfer model.

Baum et al. (2005; 2011) gives the formulas for the average scattering and extinction cross sections:

$$\sigma_{s,e} = \frac{\int_{\lambda_1}^{\lambda_2} \int_{D_{min}}^{D_{max}} \left[\sum_{h=1}^{M} \sigma_{s,e,h}(D,\lambda)f_h(D)\right] n(D)F_s(\lambda)S(\lambda)dDd\lambda}{\int_{\lambda_1}^{\lambda_2} \int_{D_{min}}^{D_{max}} \left[\sum_{h=1}^{M} f_h(D)\right] n(D)F_s(\lambda)S(\lambda)dDd\lambda} , \quad (29)$$

where the subscripts s and e indicate the scattering and extinction cross sections, respectively. The sum over h is for the mixture of ice crystal habits considered in this study (the General Habit Mix, or GHM); for a single habit this term is not needed. The habit fraction $f_h(D)$ is defined in the following way:

$$\sum_{h=1}^{M} f_h(D) = 1 , \quad (30)$$

where M is the number of habits, D is the particle diameter, n(D) is the density, $F_s(\lambda)$ is the spectral response function (SRF), and $S(\lambda)$ is the solar flux.

The satellite sensor records radiation from a certain wavelength range and is more sensitive at certain wavelengths than others. The function which describes sensitivity with wavelength is the spectral response function (SRF). The PARASOL spectral response function for the 0.865 μm band is shown in Fig. 8. This band on the PARASOL satellite records radiation from 0.804 to 0.924 μm, however the band edges are less sensitive than the center of the distribution. The final averaged scattering properties are weighted for each wavelength in the SRF and for the intensity of the sunlight seen by the sensor at each wavelength, $S(\lambda)$.

The ratio of the scattering to extinction cross sections gives the single scattering albedo $\widetilde{\omega}_0$:

$$\widetilde{\omega}_0 = \frac{\sigma_s}{\sigma_e} \; . \tag{31}$$

With no absorption, $\sigma_e = \sigma_s$ and $\widetilde{\omega}_0 = 1$.
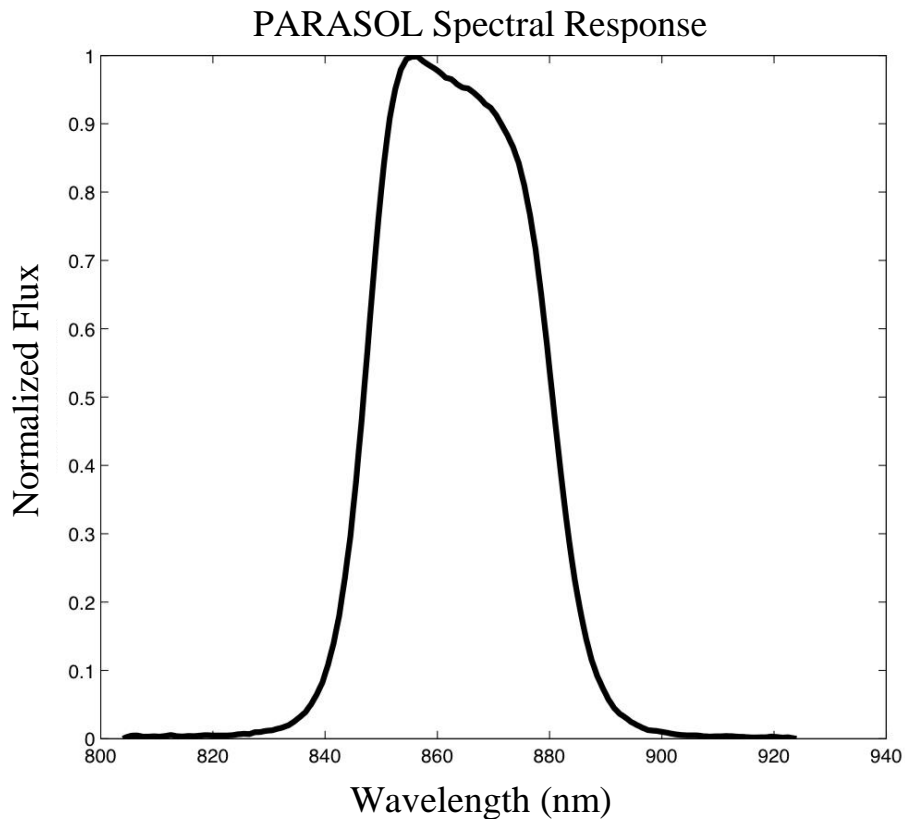
Fig. 8. Spectral Response Function for the 0.865 µm PARASOL band. Values have been normalized to the maximum observed value.

The first moment of the phase function P_{11} is called the asymmetry factor, or g, and is the weighted average of the cosine of the scattering angle for scattered radiation. It is 1 for complete forward scattering (scattering angle of $0°$, $\cos(0) = 1$) with lower values indicating more backscattering.

The average asymmetry factor over the particle size distribution (PSD) and habit distribution is found using the same method as the scattering cross section:

$$g = \frac{\int_{\lambda_1}^{\lambda_2} \int_{D_{min}}^{D_{max}} \left[\sum_{h=1}^{M} g_h(D,\lambda)\sigma_{s,h}(D,\lambda)f_h(D)\right]n(D)F_s(\lambda)S(\lambda)dDd\lambda}{\int_{\lambda_1}^{\lambda_2} \int_{D_{min}}^{D_{max}} \left[\sum_{h=1}^{M} \sigma_{s,h}(D,\lambda)f_h(D)\right]n(D)F_s(\lambda)S(\lambda)dDd\lambda} . \quad (32)$$

To get a description of the average size of ice particles in a given volume, a concept called the effective diameter D_{eff} is used. This quantity is defined as the ratio of the total volume to the total projected area (Baum et al. 2011):

$$D_{eff} = \frac{3}{2} \frac{\sum_{h=1}^{M}\left[\int_{D_{min}}^{D_{max}} V_h(D)n(h,D)dD\right]}{\sum_{h=1}^{M}\left[\int_{D_{min}}^{D_{max}} A_h(D)n(h,D)dD\right]} . \quad (33)$$

Each particle size distribution (PSD) considered in the calculations will have a characteristic effective diameter. The average single scattering phase matrix can be similarly computed:

$$P(\Theta) = \frac{\int_{\lambda_1}^{\lambda_2} \int_{D_{min}}^{D_{max}} \left[\sum_{h=1}^{M} P_h(\Theta,D,\lambda)\sigma_{s,h}(D,\lambda)f_h(D)\right]n(D)F_s(\lambda)S(\lambda)dDd\lambda}{\int_{\lambda_1}^{\lambda_2} \int_{D_{min}}^{D_{max}} \left[\sum_{h=1}^{M} \sigma_{s,h}(D,\lambda)f_h(D)\right]n(D)F_s(\lambda)S(\lambda)dDd\lambda} . \quad (34)$$

Particle Size Distributions

Nine different ice shapes and one habit mixture are used in the current study. For a single ice habit, Eq. (34) is the same, but the sum over habits is removed since only

one is considered. The bulk scattering properties are otherwise calculated in exactly the same way. For both the single habits and the GHM habit mixture, the bulk scattering properties are produced using a database of over 12,000 particle size distributions measured by various field campaigns (Baum et al. 2011). The effective diameter is calculated for each size distribution, and the scattering phase matrix, asymmetry parameter, and other single scattering properties are calculated. The result is a large database of scattering properties with an effective diameter which describes each member of the set. Single scattering properties are desired for regular intervals of effective diameter, so the results in the database which fall into predetermined size bins are averaged together to produce a set of scattering properties for a certain effective diameter. In the present study, scattering properties are calculated for effective diameters between 10 and 120 μm with bin sizes 5 μm wide.

Only three effective diameters (30, 60, and 90 μm) will be used in this study because polarization is weakly sensitive to the ice diameter. In order to include size in the analysis, it would be necessary to include observations at an infrared wavelength where ice size may be determined.

Truncation of the Forward Peak

Once the bulk scattering properties have been obtained, the forward peak of the phase function needs to be truncated (removed). Diffraction causes the scattered intensity in the forward direction (scattering angle $\Theta = 0°$) to be many orders of magnitude greater than in the backward direction (c.f. Fig. 7). This peak is hard to

represent in the adding-doubling code because it must be approximated with polynomials, so it is easier to remove it entirely.

In the radiative transfer model used in this study, the phase matrix is represented by Legendre polynomials in calculations because the expansion coefficients can be easily found using orthogonality relations and also can be added together (Liou 2002). Since the phase function is strongly peaked in the forward direction, representing it accurately with polynomials requires thousands of terms. The computational time to calculate these terms is a significant hindrance (Wiscombe 1977). There is a way to represent the phase function with a few hundred or fewer terms, however.

Truncation removes the forward diffraction peak and so reduces the number of polynomial terms necessary to approximate the phase function. The δ-fit truncation method (Hu et al. 2000), which is similar to the earlier Delta-M method (Wiscombe 1977), uses weighted singular-value decomposition least-squares fitting, allowing it to more closely follow the phase function at larger scattering angles. This method chooses polynomial coefficients based on the minimum in the squared differences between the actual phase function and the one approximated with polynomials.

When the phase function (P_{11} term of the phase matrix) is truncated, the other elements of the phase matrix must be changed in some way to be consistent with the changes in the phase function. Each of the other phase matrix elements is scaled according to Chami et al. (2001):

$$P_{22}^*(\Theta) = \frac{P_{22}}{P_{11}} P_{11}^*(\Theta) \, , \tag{35}$$

where the asterisk denotes the element after it has been truncated. The similarity

principle states that the optical thickness, single scattering albedo, asymmetry parameter

g, and other scattering properties must also be scaled when the phase function is

truncated (Liou 2002). The truncated asymmetry parameter can be written:

$$g^* = \frac{g-f}{1-f} \, ,$$

(36)

where here f is the portion of scattered energy in the truncated forward peak. The single

scattering albedo and optical thickness are given by:

$$\widetilde{\omega}_0^* = \frac{(1-f)\widetilde{\omega}_0}{(1-f\widetilde{\omega}_0)} \, ,$$

(37)

$$\tau^* = (1 - f\widetilde{\omega}_0)\tau \, .$$

(38)

All of the reported values for the phase matrix, optical thickness, single scattering

albedo, and asymmetry parameter *g* used in later sections will be the truncated values.

CHAPTER IV

PARASOL DATA AND SATELLITE BACKGROUND

PARASOL (Polarization and Anisotropy of Reflectances for Atmospheric Sciences coupled with Observations from a Lidar) is a French microsatellite which was launched in 2004 to study the radiative and microphysical properties of clouds and aerosols and improve our understanding of climate. The instrument on board is a wide-field imaging radiometer/polarimeter named POLDER (POLarization and Directionality of the Earth's Reflectances), capable of retrieving the I, Q, and U Stokes parameters at up to 16 viewing angles for each pixel (Breon 2009). The Level-2 data is used in this study, a product which includes parameters of interest including surface type, percentage cloud cover, optical thickness, and thermodynamic phase. In order to select pixels for use in this study, many different parameters will be used to filter the available data.

Instrument Design

The imager is a CCD matrix and has a rotating wheel with spectral filters and polarizers for a total of nine channels, three of which include polarization measurements, including the 0.865 μm channel used in the present study. In order to collect the I, Q, and U Stokes parameters three measurements are necessary with the polarizer axis turned by 60° for each measurement. To counteract the effect of spacecraft movement during these polarization measurements a small angle wedge prism is employed for each polarizer (Breon 2006).
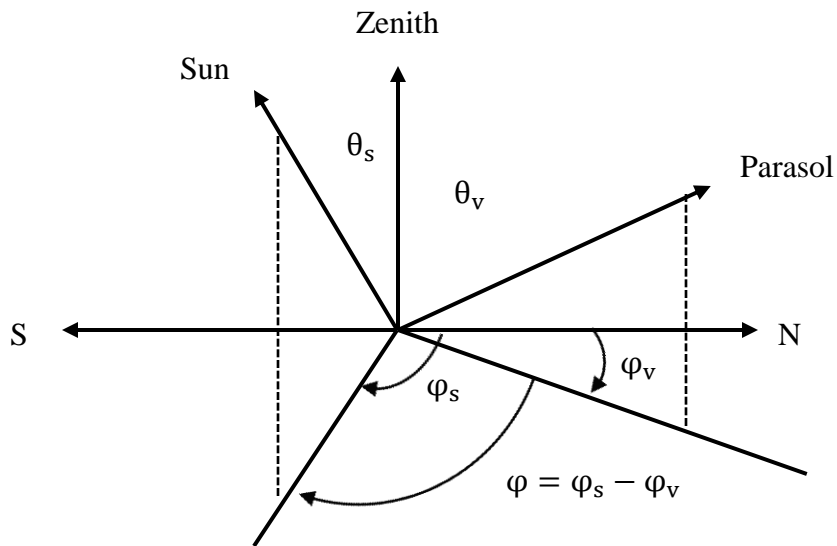
Fig. 9. Coordinate system for PARASOL observations. θ_s is the solar zenith angle, θ_v the viewing zenith angle, and ϕ the relative azimuth angle.
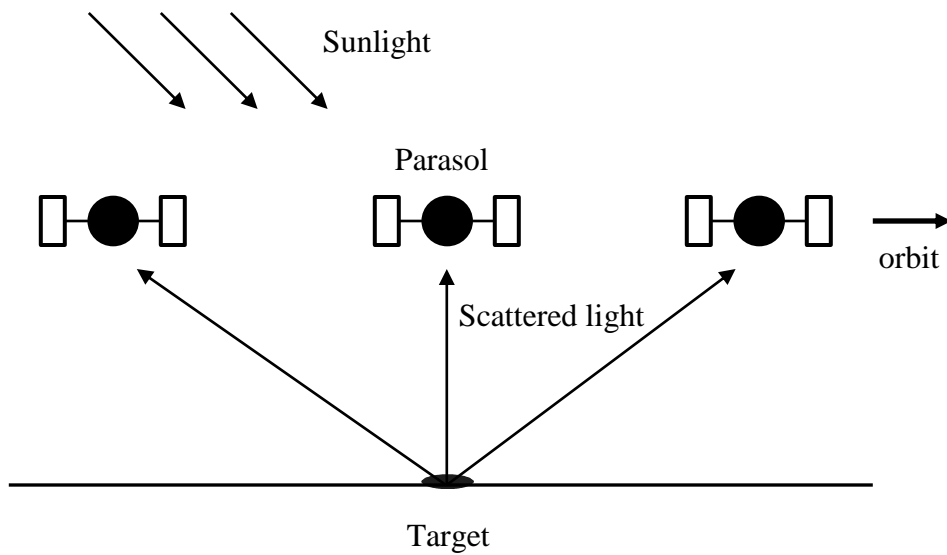
Fig. 10. Viewing geometry of the PARASOL satellite. This shows how measurements are obtained at multiple scattering angles.

Multi-Angle Capability

Fig. 10 shows how PARASOL achieves its multi-angle capability. The satellite can view the same scene from many different angles as it flies overhead, allowing the same pixel to have measurements at up to 16 distinct scattering angles. The viewing zenith angle is defined with respect to the local zenith and varies between $0°$ and $75°$ in the PARASOL data. The solar zenith angle also is defined from the local zenith and varies between $0°$ and $80°$ in the PARASOL observations. The relative azimuth angle is defined with respect to the local north direction and varies between $0°$ and $360°$ in observations. According to this definition, $180°$ is forward scattering, and $0°$ or $360°$ is backscattering. See Fig. 9 for the geometry involved.

The Level-2 Cloud Product

The PARASOL Level-2 cloud product is produced by processing the Level-1 radiances by CNES (Centre National d'Etudes Spatiales) to generate useful parameters for the study of cloud microphysics. The parameters used in this study are percentage cloud cover, surface type, optical thickness, thermodynamic phase, and normalized, modified, polarized radiance at 0.865 μm. The normalized, modified, polarized radiance is defined in the following way (C.-Labonnote et al. 2001):

$$L_{nmp}(\theta_v, \varphi_v, \theta_s, \varphi_s) = \frac{\pi L_p}{E_s} \frac{\cos\theta_s + \cos\theta_v}{\cos\theta_s}, \tag{39}$$

where subscript s is for the solar zenith and azimuth angles, and subscript v is for the viewing angles. E_s is the incident solar flux at the top of the atmosphere. L_p is the polarized radiance, defined as:

$$L_p = \pm\sqrt{Q^2 + U^2}. \tag{40}$$

In order to compare satellite measurements with modeling results, the adding-doubling radiative transfer model produces Stokes parameters for the simulated ice cloud and calculates the polarized radiance in the same way as the PARASOL satellite. The satellite and simulated results can then be used in the retrieval of ice habit and roughness.

Restrictions are placed on the data used in the current study. To get a full picture of the scattering, the range of scattering angles for each pixel must be at least $50°$. In addition, the number of viewing directions with available data (out of the 16 possible directions) must be at least seven, and the PARASOL scene has to be over the ocean.

The ocean surface is dark and almost non-polarizing at 0.865 μm, and so is simple to model in radiative transfer codes. The restriction on the range of scattering angles allows broad features in the polarization pattern to be observed for each pixel, which then allows distinctions to be made among different ice models based on their fit to this polarization. Because this study focuses on ice clouds, a pixel must be marked as 100% cloudy and its phase must be marked as ice in the Level-2 cloud product to be included. Measurements in the sunglint region which is near the solar principal plane (the plane containing the incident solar zenith direction) are not included because the polarization is large and would overwhelm and polarization signal from an ice cloud. Data from 1 January 2007, 1 April 2007, August 1, 2007, and 15 October 2007 are used that come from 14-15 orbits of the satellite. After applying the necessary filters, about 50,000 - 70,000 data points are left from each month of data for use in comparison studies with modeled data.

CHAPTER V

RADIATIVE TRANSFER MODEL

In order to calculate the vector intensity of scattered radiation from an ice cloud at the top of the atmosphere a model must be employed to calculate the transfer of radiation through the ice cloud layer. In the case of this study, a plane-parallel method is used where the cloud is considered as a some finite number of horizontal layers, infinite in extent. Within the plane-parallel assumption, the adding method and the doubling method are used to calculate scattered intensity. Van de Hulst (1980) presented the equations for the two methods and has a comprehensive overview of their utility. The radiative transfer code used in this study was written at the Free University of Amsterdam by de Haan et al. (1987) and provides the vector intensity and polarization of radiation at the top (or bottom) of a plane-parallel model.

The Adding Method

The atmosphere can be separated into many plane-parallel layers with different layers for clouds and atmospheric gases. Fig. 11 illustrates the concept for two atmospheric layers with . What is desired is the reflection and transmission matrices (**R**,**T**) for the combined system. The adding method is a set of equations which allows the reflection and transmission matrices of the combined system to be found if the matrices for the individual layers are known.

Fig. 11. The adding method. Illustration of a plane parallel system showing how radiation incoming from above layer 1 will reflect at layer 1 or transmit through and then reflect at layer 2 or transmit through. Infinite reflections can occur at the interface between the two layers, but become negligible after several reflections.

In most cases the reflection and transmission matrices are not known and must be determined from the optical thickness and properties of the individual layer. To get these matrices, each layer must be divided into sub-layers thin enough so that it can be considered homogeneous and scattering can be approximated by either one or two orders of scattering, significantly decreasing the computational time that the calculation requires.

Once the reflection and transmission matrices have been calculated for the thin layers, the adding equations can be used to find the combined matrices and the process continues until the original optical thickness of the layer for which scattered intensity is desired has been obtained. Multiple scattering is included in this method by considering the infinite reflections that can occur at the interface between two layers, an effect fully incorporated into the reflection and transmission matrices.

The Doubling Method

When the layer considered does not have properties which vary with optical thickness, then the doubling method can provide a faster way to calculate the reflection and transmission matrices. The large layer is divided into layers thin enough to approximate with one or two orders of scattering like in the adding method, but because the properties of each thin layer are the same, the reflection and transmission matrices do not need to be recalculated each time. Instead, layers can be added together two at a time using the adding equations until the optical thickness of the original layer is reached. The only restriction on the doubling method is that the thin layers approximated with one or

two orders of scattering must be the same optical thickness so that the reflection and transmission matrices are exactly the same.

For the current study a three-level atmosphere was employed. The top layer consists only of Rayleigh scatterers, the middle layer has a single-layer ice cloud, and the bottom layer is also composed solely of Rayleigh scatterers. A standard mid-latitude summer atmospheric profile was used and the Rayleigh scattering depolarization factor used in the adding-doubling model is 0.0279, as reported in Young (1980). The Rayleigh optical depth for each layer is taken from the tables in Tomasi et al. (2005). Since each individual layer of cloud or Rayleigh gases is vertically homogeneous, the doubling method may be used to obtain the reflection and transmission matrices, and the adding method used to calculate the total reflection and transmission from the combined system.

The Adding Equations

A summary of the equations for adding and doubling are presented in this section. This summary follows that of de Haan et al. (1987), and further explanations, illustrations, and equations can be found therein. To keep track of radiation propagating both upward and downward through a plane-parallel system, de Haan et al. (1987) use the matrices $\mathbf{U}(\tau, \mu, \mu', \varphi - \varphi')$ and $\mathbf{D}(\tau, \mu, \mu', \varphi - \varphi')$, defined by the following equations:

$$\mathbf{I}(\tau, -\mu, \varphi) = \frac{1}{\pi} \int_0^{2\pi} \int_0^1 \mathbf{U}(\tau, \mu, \mu', \varphi - \varphi') \mathbf{I}(0, \mu', \varphi') \mu' d\mu' d\varphi' \quad , \qquad (41)$$

$$\mathbf{I}(\tau, \mu, \varphi) = \frac{1}{\pi} \int_0^{2\pi} \int_0^1 \mathbf{D}(\tau, \mu, \mu', \varphi - \varphi') \mathbf{I}(0, \mu', \varphi') \mu' d\mu' d\varphi'$$

$$+ \exp\left[-\frac{\tau}{\mu}\right] \mathbf{I}(0, \mu, \varphi) \quad , \qquad (42)$$

where $\mathbf{I}(0, \mu, \varphi)$ is the incident intensity at TOA. Eqs. (41) and (42) provide the upward

and downward intensity as a function of optical thickness in plane parallel system. The

direct radiation beam unscattered by the layer and reaching an arbitrary optical thickness

τ is represented by the exponential term in Eq. (42).

The desired result is to be able to calculate the matrices $\mathbf{U}$ and $\mathbf{D}$ from the albedo

$\widetilde{\omega}_0$ and phase matrix $\mathbf{Z}(\tau,\mu,\mu',\varphi - \varphi')$. $\mathbf{Z}$ is the scattering phase matrix as defined in the

meridian plane. The adding equations will allow the calculation of $\mathbf{U}$ and $\mathbf{D}$ from the

albedo $\widetilde{\omega}_0$ and the scattering phase matrix $\mathbf{Z}$.

In this study the Stokes vector at TOA must be the output from the method since

comparison with the measured Stokes vector from satellite data is desired. $\mathbf{U}$ and $\mathbf{D}$ at

the top of the plane parallel layer are then just determined by their boundary values, and

the boundary value matrices are simply the reflection and transmission matrices. They

can be written as the following:

$$\mathbf{T}(\mu, \mu', \varphi - \varphi') = \mathbf{D}(\tau', \mu, \mu', \varphi - \varphi')$$

$$\mathbf{R}(\mu, \mu', \varphi - \varphi') = \mathbf{U}(0, \mu, \mu', \varphi - \varphi')$$

$$\mathbf{T}^*(\mu, \mu', \varphi - \varphi') = \mathbf{D}^*(0, \mu, \mu', \varphi - \varphi')$$

$$\mathbf{R}^*(\mu, \mu', \varphi - \varphi') = \mathbf{U}^*(\tau', \mu, \mu', \varphi - \varphi') . \qquad (43)$$

The radiation from below the layer is denoted with an asterisk, while τ' indicates the

entire optical depth, with $\tau = 0$ being the top of the layer. Two assumptions then are

needed. If no reflecting surface is present and if all layers are homogeneous and can be

approximated with one or two orders of scattering, then the reflection and transmission

matrices can be found with the following equations:

$$\mathbf{R}(\mu, \mu', \varphi - \varphi') = \frac{\widetilde{\omega}_0}{4(\mu + \mu')} \mathbf{Z}(\mu, \mu', \varphi - \varphi')\left(1 - \exp\left[-\tau'\left(\frac{1}{\mu} + \frac{1}{\mu'}\right)\right]\right), \quad (44)$$

$$\mathbf{T}(\mu, \mu', \varphi - \varphi') = \frac{\widetilde{\omega}_0}{4(\mu + \mu')} \mathbf{Z}(\mu, \mu', \varphi - \varphi')\left(\exp\left[-\tau'\left(\frac{1}{\mu}\right)\right] - \exp\left[-\tau'\left(\frac{1}{\mu'}\right)\right]\right), \text{ if } \mu \neq \mu'$$

$$\mathbf{T}(\mu, \mu', \varphi - \varphi') = \frac{\widetilde{\omega}_0 \tau'}{4\mu^2} \mathbf{Z}(\mu, \mu', \varphi - \varphi')\exp[-\tau'\left(\frac{1}{\mu}\right)] \ . \qquad (45)$$

In order to calculate the infinite reflections which can occur between layers these three

equations are used:

$$\mathbf{Q}_1(\mu, \mu', \varphi - \varphi') = \frac{1}{\pi} \int_0^{2\pi} \int_0^1 \mathbf{R}'^*(\mu, \mu'', \varphi - \varphi'')\mathbf{R}''(\mu'', \mu', \varphi'' - \varphi')\mu''d\mu''d\varphi''$$

$$\mathbf{Q}_{n+1}(\mu, \mu', \varphi - \varphi') = \frac{1}{\pi} \int_0^{2\pi} \int_0^1 \mathbf{Q}_1(\mu, \mu'', \varphi - \varphi'')\mathbf{Q}_n(\mu'', \mu', \varphi'' - \varphi')\mu''d\mu''d\varphi''$$

$$\mathbf{Q}(\mu, \mu', \varphi - \varphi') = \sum_{n=1}^{\infty} \mathbf{Q}_n(\mu, \mu', \varphi - \varphi') \ . \qquad (46)$$

Here a single prime denotes the top layer, while a double prime denotes the bottom

layer. The first equation for $\mathbf{Q}_1$ integrates the reflection matrix from the bottom layer

(radiation from above) multiplied by the reflection matrix from the top layer (radiation

from below) over all solid angles. The integration finds the contribution of scattering in a

certain direction (μ, φ). The sum over $\mathbf{Q}_n$ adds up all of the (possibly infinite) reflections

between the two layers and also considers the number of times n that the beam crosses

the combined layer going in the upward direction.

With all of these results the matrices $\mathbf{U}$ and $\mathbf{D}$ (for radiation going up or down) in the combined layer can be written:

$$\mathbf{D} = \mathbf{T} + \mathbf{Q} \exp\left[-\tau'\left(\frac{1}{\mu'}\right)\right] + \mathbf{QT}$$

$$\mathbf{U} = \mathbf{R} \exp\left[-\tau'\left(\frac{1}{\mu'}\right)\right] + \mathbf{RD} . \tag{47}$$

Note that layers with the same optical thickness and single scattering properties have been used and in addition the layers are homogeneous. The notation is also simplified, meaning that the final terms in both equations are an integration as in Eq. (46).

The reflection and transmission matrices for the combined layer are the desired result. These can be found with the following equations:

$$\mathbf{R}(\mu, \mu', \varphi - \varphi') = \mathbf{R}(\mu, \mu', \varphi - \varphi') + \mathbf{U}(\tau', \mu, \mu', \varphi - \varphi') \exp\left[-\tau'\left(\frac{1}{\mu}\right)\right]$$

$$+ \frac{1}{\pi} \int_0^{2\pi} \int_0^1 \mathbf{T}^*(\mu, \mu'', \varphi - \varphi'') \mathbf{U}(\tau', \mu'', \mu', \varphi'' - \varphi') \mu'' d\mu'' d\varphi'' , \tag{48}$$

$$\mathbf{T}(\mu, \mu', \varphi - \varphi') = \mathbf{T}''(\mu, \mu', \varphi - \varphi') \exp\left[-\tau'\left(\frac{1}{\mu'}\right)\right] + \mathbf{D}(\tau', \mu, \mu', \varphi - \varphi') \exp\left[-\tau'\left(\frac{1}{\mu}\right)\right]$$

$$+ \frac{1}{\pi} \int_0^{2\pi} \int_0^1 \mathbf{T}''(\mu, \mu'', \varphi - \varphi'') \mathbf{D}(\tau', \mu'', \mu', \varphi'' - \varphi') \mu'' d\mu'' d\varphi'' . \tag{49}$$

To obtain $\mathbf{R}^*$ and $\mathbf{T}^*$ it is unnecessary to derive similar equations. A convenient symmetry relationship exists, as shown in de Haan et al. (1987):

$$\mathbf{R}^*(\mu, \mu', \varphi - \varphi') = \mathbf{R}(\mu, \mu', \varphi' - \varphi)$$

$$\mathbf{T}^*(\mu, \mu', \varphi - \varphi') = \mathbf{T}(\mu, \mu', \varphi' - \varphi) . \tag{50}$$

If identical homogeneous layers are considered then the adding equations as shown above can be repeatedly applied to add together layers until the full optical thickness of the plane parallel system to be modeled is met.

Expansion of Azimuth Dependent Functions

When using the adding equations to compute the reflection and transmission matrices of a plane parallel system, the computational time required to calculate the integrals of the azimuth-dependent functions can be very great. To reduce the computational time needed, each function dependent on the azimuth angle can be expanded in a Fourier series. The general form of the expansion is:

$$\mathbf{Z}(\mu, \mu', \varphi - \varphi') = \sum_{m=0}^{\infty} (2 - \delta_{m,0})[\mathbf{Z}^{cm}(\mu, \mu') \cos m(\varphi - \varphi')$$

$$+ \mathbf{Z}^{sm}(\mu, \mu') \sin m(\varphi - \varphi')] , \tag{51}$$

where $\mathbf{Z}$ could be any of the matrices from the adding equations and $\delta_{m,0}$ is the kronecker delta. There still needs to be some way to find the Fourier coefficients. $\mathbf{Z}^{sm}$ and $\mathbf{Z}^{cm}$ can be found from the following recurrence relation:

$$\mathbf{Z}^m(\pm\mu, \mu') = (-1)^m \sum_{l=m}^{\infty} \mathbf{P}_m^l (\pm\mu) \mathbf{S}^l \mathbf{P}_m^l(\mu) , \tag{52}$$

where $\mathbf{S}^l$ are the expansion coefficients of the phase matrix in generalized spherical functions, and $\mathbf{P}_m^l$ is a matrix of generalized spherical functions. Generalized spherical functions are the more general form of the Legendre polynomials and have the same orthogonality and addition relationships which make them useful for polynomial expansions in numerical calculations. Jackson (1998) has a more comprehensive introduction and overview of generalized spherical functions.

CHAPTER VI

RESULTS

The adding-doubling radiative transfer model calculates the top of atmosphere

TOA Stokes vector from which the polarized reflectance is obtained for a given ice

model input. Simulations were performed for 17 levels of roughness and 9 different ice

habits plus one ice habit mixture. In addition, optical thickness was considered for

thicknesses below 5, because at 5 and above the polarization is saturated and optical

thickness does not affect the results. The simulations were stored in a lookup table for

use in the retrieval algorithm.

The retrieval algorithm minimizes the difference between the observed polarized

reflectance from PARASOL and the simulation data. First the optical thickness is

estimated based on the total reflectance at 0.865 μm, and then the simulated polarized

reflectance for all possible combinations of habit and roughness is calculated. The

smallest RRMSE corresponds to the retrieved habit and roughness.

The output from the retrieval is a dataset consisting of the retrieved ice particle

habit and surface roughness for each pixel in the PARASOL dataset. Four different

months of data are considered with one full day of global observations for each month.

The days are 1 January, 1 April, 1 August, and 15 October 2007. The number of

retrieved pixels for each month is between 50,000 and 70,000**.** Table 2 shows the total

number of pixels for each month as well as the number of pixels located in each latitude

band for which results will be shown. The tropics are defined as less than 30 degrees

Table 2. Number of PARASOL pixels considered for each day of data.

	1 January 2007	1 April 2007	1 August 2007	15 October 2007
Total	54214	67264	69481	63463
Tropics	19264	11881	18580	13182
Midlatitudes	30278	42660	40169	41936
Polar	4468	12719	10732	8345

north or south latitude, the midlatitudes are defined as 30-60 N and 30-60S, and the polar

regions are defined as > 60N or > 60S. Because of restraints on surface type, scattering

angle, and orbital characteristics, most of the observed pixels are in the midlatitude

regions.

To provide some intuition for the retrieval results that follow, polarized

reflectance for several different ice shapes is plotted against PARASOL polarized

reflectance from 1 August 2007. An ice cloud of optical thickness 5 was used for all

simulations, and 20,000 viewing geometries taken from the PARASOL observations

were used in the adding-doubling model simulations.

The figures on the following pages are arranged in the following way: first the

polarized reflectance simulated using single ice habits will be plotted against density of

PARASOL polarized reflectance to develop some intuition for the behavior of the

polarized reflectance for different ice habits and levels of roughness. After that,

histograms of retrieved parameters will be shown. First retrievals of ice habit will be

examined using global data from 4 different months of the year. Retrievals of habit done for latitude bands will be examined to see if there is any dependence on latitude, and then histograms of retrieved habit assuming different ice effective diameters will be looked at to investigate the size dependence of the retrieved habit.

The same structure will be followed for presenting histograms of retrieved ice roughness: global retrieval results for 4 different months of data, then results separated by latitude, then size dependence of the roughness retrievals. Finally, histograms of the retrieved habit for pixels which are retrieved as either smooth or rough are shown to see if any ice habits are predominantly smooth or rough.

A global best fit of ice habit and roughness is also selected from the retrieval results, and a plot of its polarized reflectance as well as full single scattering phase matrix is shown.

Fig. 12 shows the polarized reflectance plotted for the solid column ice habit. Colored contours are the density of PARASOL polarized reflectance, and the black dots are simulations. Each black dot corresponds to the polarized reflectance simulated using one viewing geometry, and the spread in the simulation points is due to multiple viewing geometries corresponding to the same scattering angle. For the smooth case in the top left panel, there are many features in the simulations which are not found in the observations. The trend of the PARASOL observations is linearly decreasing polarized reflectance with scattering angle, but this cannot be reproduced by the smooth model.
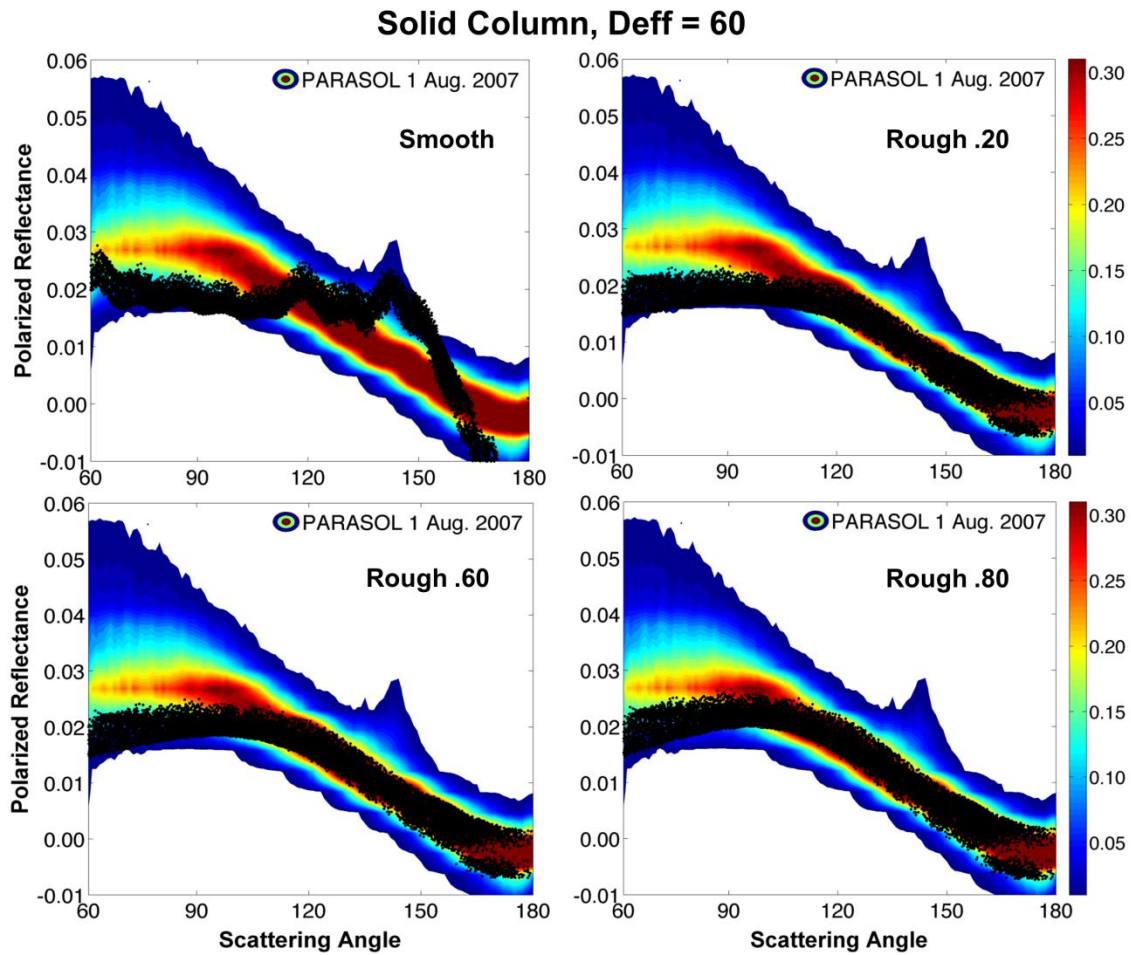
Fig. 12. Polarized reflectance simulated for solid columns. The effective diameter is 60 μm, and the ice cloud optical thickness is 5. Color contours are density of PARASOL polarized reflectance observations, and black dots are simulations. Each dot represents a calculation of polarized reflectance for a single viewing geometry.

If surface roughness is considered, many of the features of the smooth model disappear. The top right panel of Fig. 12 shows that for a roughness value of $\sigma = 0.20$, the polarized reflectance matches the observations except at small scattering angles. The oscillatory features in the smooth case are not seen and the decreasing trend is reproduced. The bottom two panels of Fig. 12 show increasing levels of roughness, but the results do not change appreciably, except for angles near 100 degrees. A roughness value of $\sigma = 0.8$ corresponds to the maximum value of roughness used in the retrieval.

Fig. 13 shows the same type of plot for the aggregate of columns ice habit. Because this habit is composed of columns arranged in a compact structure, its simulated polarized reflectance is very similar to the single solid column. The results follow the same pattern but are slightly more tightly gathered at large scattering angles between 120 and 150 degrees. Examining plots like this qualitatively does not allow for rigorous determination of the best ice habit when polarized reflectance patterns are so similar.

Fig. 14 shows polarized reflectance for the hollow column ice habit. The polarized reflectance signature is very different for this case even though the shape is the same because the center of the column is hollowed out. The top left panel shows the smooth case, where polarization is much too high. The oscillatory features seen in the solid column case are not seen here because of the hollow center, which acts to smooth out the scattering pattern in much the same way that surface roughness does (C.-Labonnote et al. 2001).
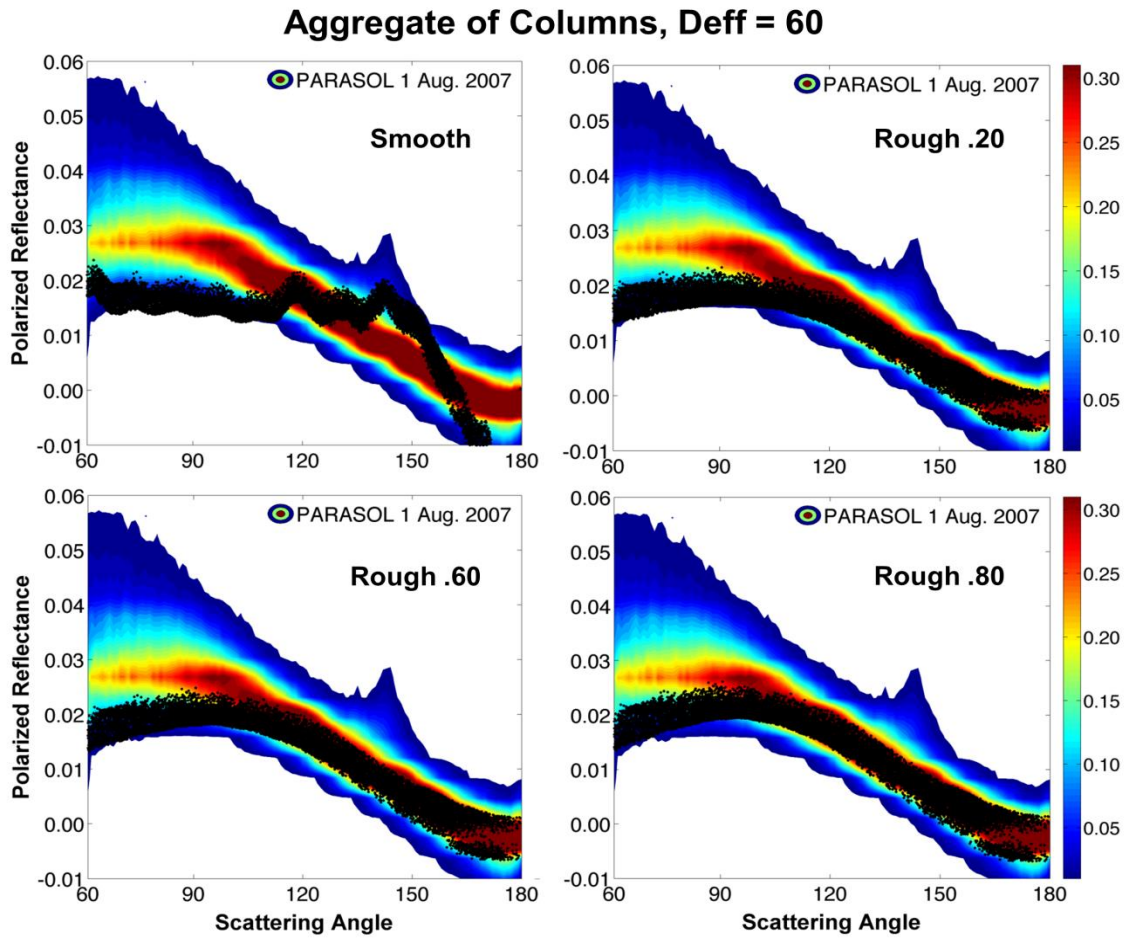
Aggregate of Columns, Deff = 60

Fig. 13. Polarized reflectance simulated for a compact aggregate of solid columns. The effective diameter is 60 μm, and the ice cloud optical thickness is 5. Color contours are density of PARASOL polarized reflectance observations, and black dots are simulations. Each dot represents a calculation of polarized reflectance for a single viewing geometry.
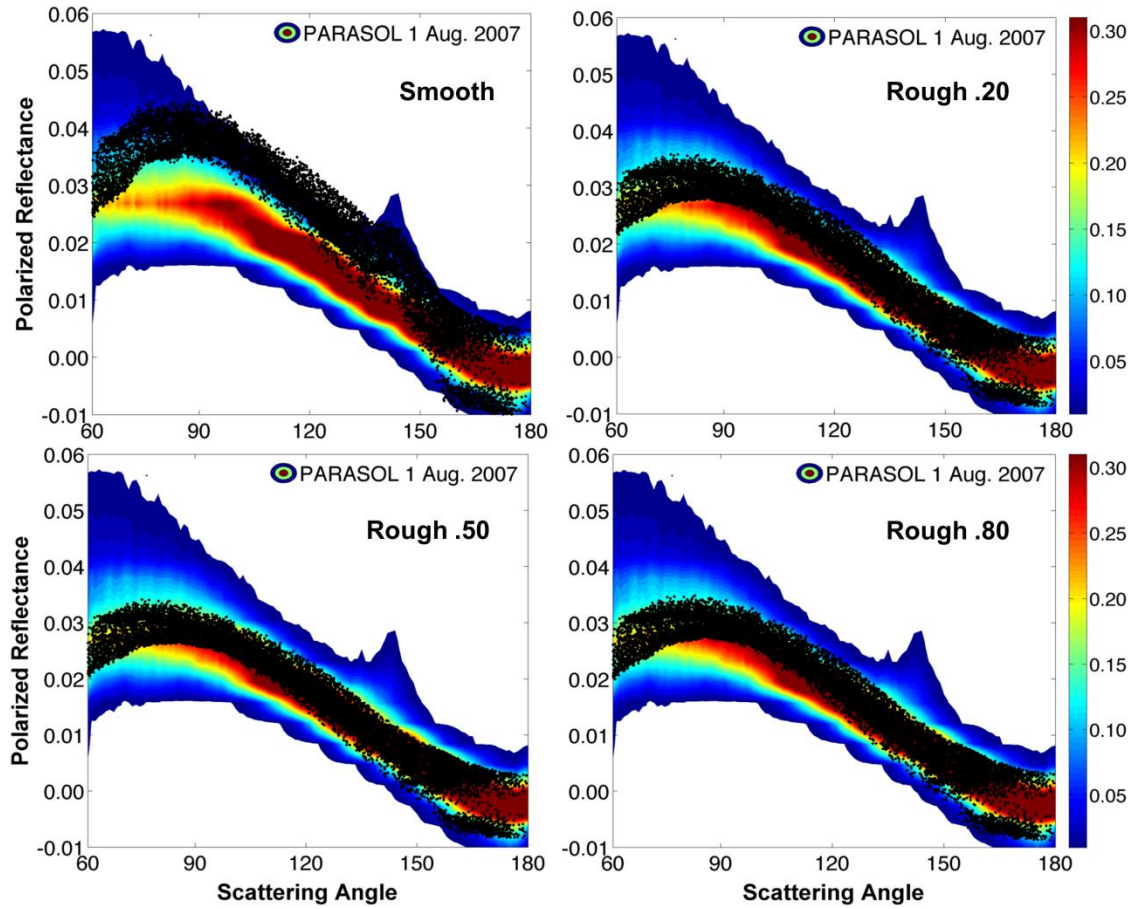
Hollow Column, Deff = 60

Fig. 14. Polarized reflectance simulated for hollow columns. The effective diameter is 60 μm, and the ice cloud optical thickness is 5. Color contours are density of PARASOL polarized reflectance observations, and black dots are simulations. Each dot represents a calculation of polarized reflectance for a single viewing geometry.

The top right panel shows a moderate level of surface roughening added which causes the polarization to decrease, and the same pattern is seen for the bottom two panels as well, which show increased surface roughening. The hollow column does not provide as good a match to PARASOL at scattering angles from 150 to 180 degrees as the solid column or aggregate of columns does. The spreading of results near these scattering angles is due to the polarized reflectance approaching zero at the neutral point in the atmosphere. The neutral point is where both the Q and U components of the Stokes vector are zero. When Q and U are near zero, the definition of polarized reflection makes these values diverge from zero, and this effect can be seen in Fig. 14.

Fig. 15 shows polarized reflectance for the small quasi-spherical droxtal ice habit. Results are similar to the previous three plots, but with an interesting feature near 120 degrees scattering angle that does not get smoothed out with increasing roughness. True spherical particles have a minimum in the phase function near this angle, causing a local maximum in the polarization. Since droxtals are quasi-spherical a less pronounced bump is seen as in Fig. 15.

Results for polarized reflectance simulated using a 5-member spatial aggregate of plates are shown in Fig. 16. The only difference here is higher polarization at small scattering angles for the smooth case, and greater spread in the measurements at large scattering angles.
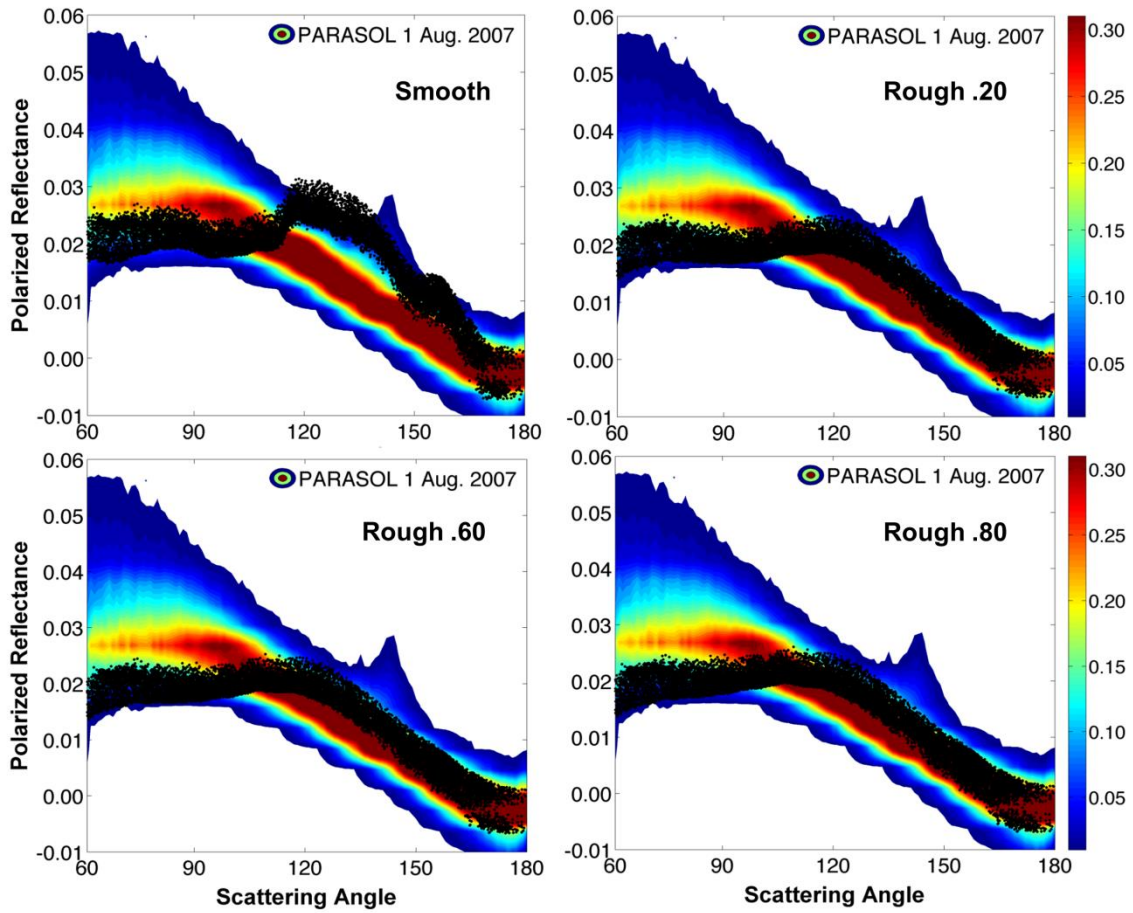
Droxtal, Deff = 60

Fig. 15. Polarized reflectance simulated for droxtals. The effective diameter is 60 μm, and the ice cloud optical thickness is 5. Color contours are density of PARASOL polarized reflectance observations, and black dots are simulations. Each dot represents a calculation of polarized reflectance for a single viewing geometry.
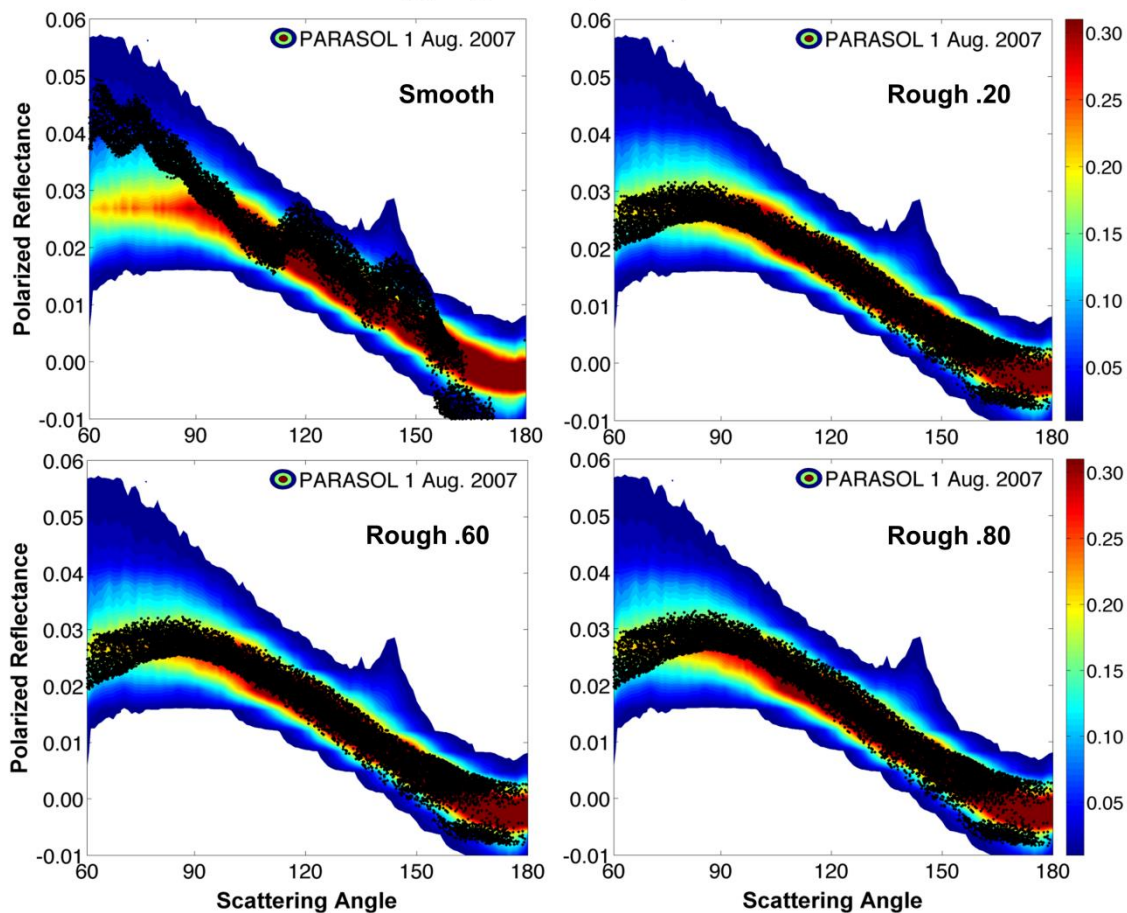
Small aggregate of plates, Deff = 60

Fig. 16. Polarized reflectance simulated for a 5 member spatial aggregate of plates. The effective diameter is 60 μm, and the ice cloud optical thickness is 5. Color contours are density of PARASOL polarized reflectance observations, and black dots are simulations. Each dot represents a calculation of polarized reflectance for a single viewing geometry.

From the previous five figures it can be seen that at least qualitatively, roughness improves the fit to polarized reflectance seen from PARASOL, but it is not possible to select a single habit that provides the best fit. To explore the fit of polarization further, results from a quantitative retrieval of habit and roughness will now be shown.

For each day of global data from the 4 months considered, the retrieval algorithm calculated the polarized reflectance for all possible combinations of habit and roughness when retrieving a single pixel. Each pixel can have up to 16 viewing directions, all of which are considered in retrieving the single pixel. This provides a wide range of scattering angles to consider when selecting the best habit and roughness.

The follow histogram plots first show the retrieved habit for 1 day of global data out of four separate months of the year, then also retrieved habit from separate latitude bands. Then the retrieved roughness is shown for the same conditions, and plots of sensitivity of retrieved habit and roughness to ice effective diameter are also shown.

Fig. 17 is a histogram of the retrieved ice habit for PARASOL data from different months of the year, for an effective ice particle diameter of 60 μm. This is nearly the mean effective diameter retrieved for ice from MODIS (Mace et al. 2005) The ordinate is the fraction of total pixels, and the abscissa shows the 10 different single ice habits and 1 mixture that are considered in the retrieval. The aggregate of columns dominates the retrieved pixels, with a consistent 65-75% of pixels across the year. Solid columns and hollow columns contribute another 15-20%, with small fractions also of solid 3D bullet rosettes and a 5-member spatial aggregate of plates. None of the other shapes has a meaningful number of retrieved pixels.
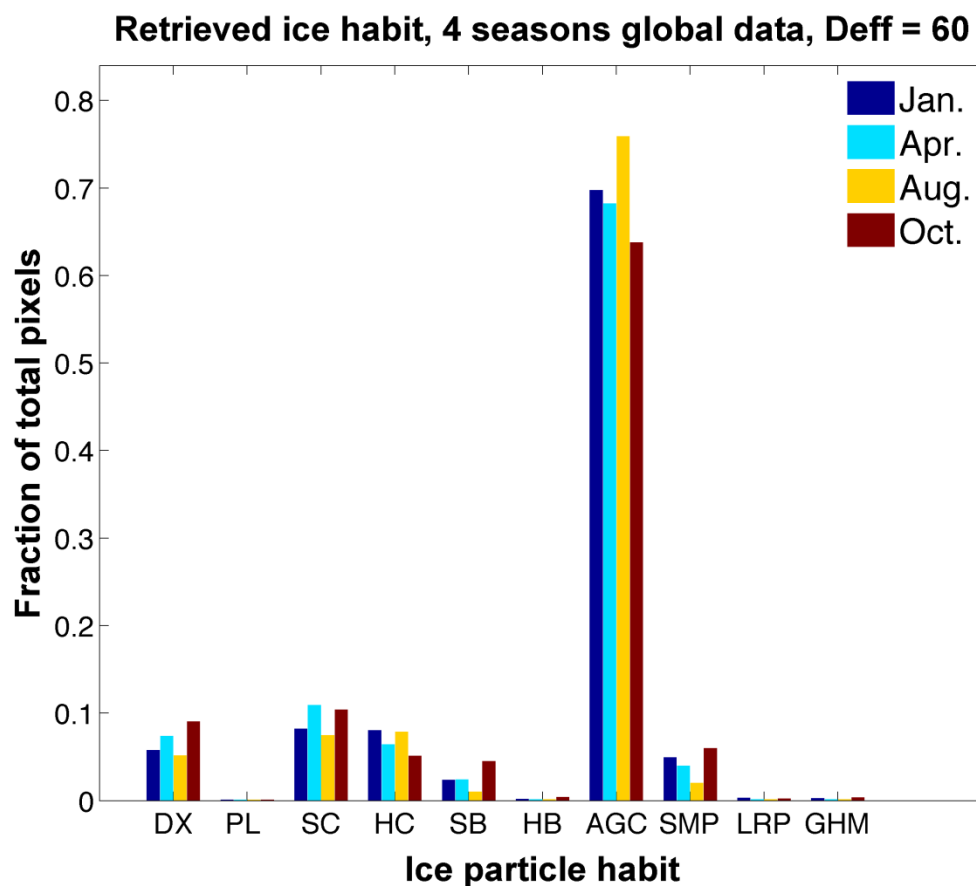
Fig. 17. Global retrieved ice habit. This shows a histogram of the fraction of total pixels retrieved as one of the 9 single habits or habit mixture, shown for data from 4 different months. DX = droxtal, PL = plate, SC = solid column, HC = hollow column, SB = solid bullet rosette, HB = hollow bullet rosette, AGC = compact aggregate of columns, SMP = 5 member spatial aggregate of plates, LRP = 10-member spatial aggregate of plates, and GHM = General Habit Mix.
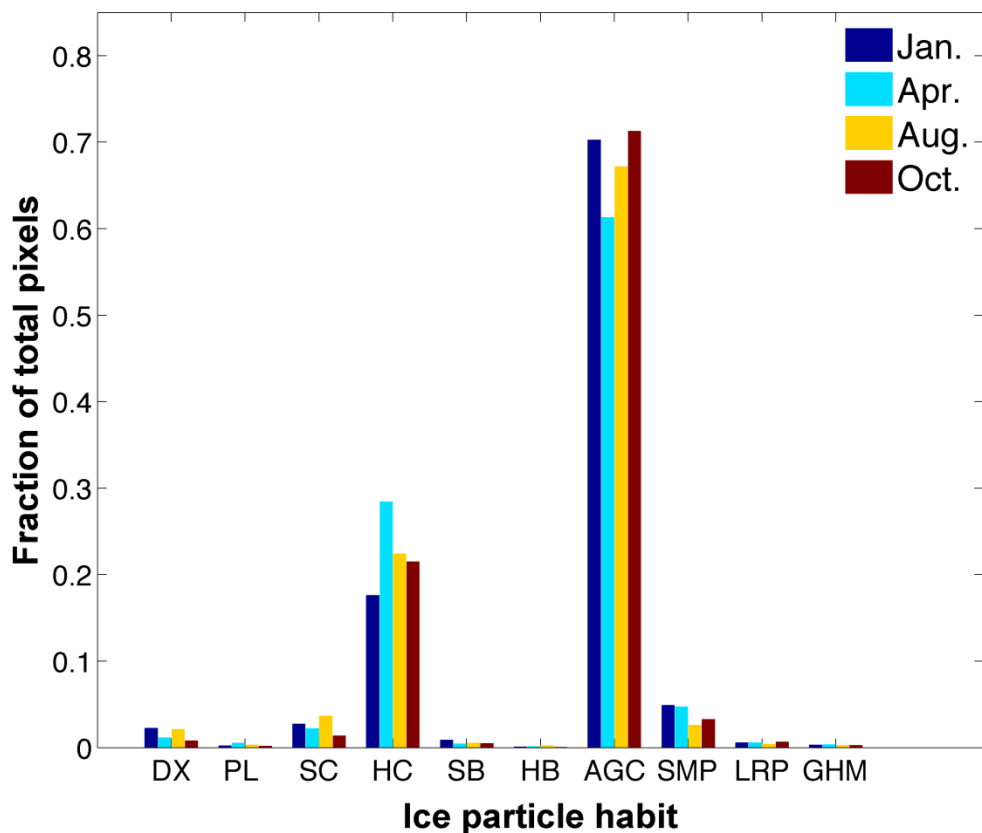
Fig. 18. Ice habit retrieved in tropical regions. This shows a histogram of the fraction of total pixels retrieved as one of the 9 single habits or habit mixture, shown for data from 4 different months in tropical regions only. DX = droxtal, PL = plate, SC = solid column, HC = hollow column, SB = solid bullet rosette, HB = hollow bullet rosette, AGC = compact aggregate of columns, SMP = 5 member spatial aggregate of plates, LRP = 10-member spatial aggregate of plates, and GHM = General Habit Mix.

Looking at the retrieved habit as a function of latitude bands, Fig. 18 shows results for the tropics, both the northern and southern hemisphere. Two habits dominate, the compact aggregate of columns and hollow columns. Aggregates comprise the same fraction of the total retrievals at 60-70%. Hollow columns are 20% or slightly more for most months and the 5-member aggregate of plates is less than 5% in all cases.

Fig. 19 and Fig. 20 show the retrieved habit for the midlatitudes and the polar regions, respectively. The midlatitude retrievals and polar retrievals again show the aggregate of columns dominating, though in the polar regions the percentage falls to 60% or slightly below. Droxtals make up a larger fraction of the retrieved habit for PARASOL pixels located in polar regions, from 15% to nearly 20% for data from January.

To investigate the sensitivity of the retrieval of habit to the ice effective diameter, Fig. 21 shows the retrieved habit for three different effective diameters, 30, 60, and 90 µm. 30 µm is smaller than the mean ice size retrieved from MODIS, 60 is near the mean, and 90 is larger. The PARASOL global dataset from 1 August 2007 was used for this case. Little sensitivity to size is seen and most retrieved habits are within a few percent for each size. Fig. 22 shows the same plot, but using PARASOL data from 1 January 2007. In this case as well, the retrieval returns nearly the same habit fractions no matter what ice effective diameter is used.
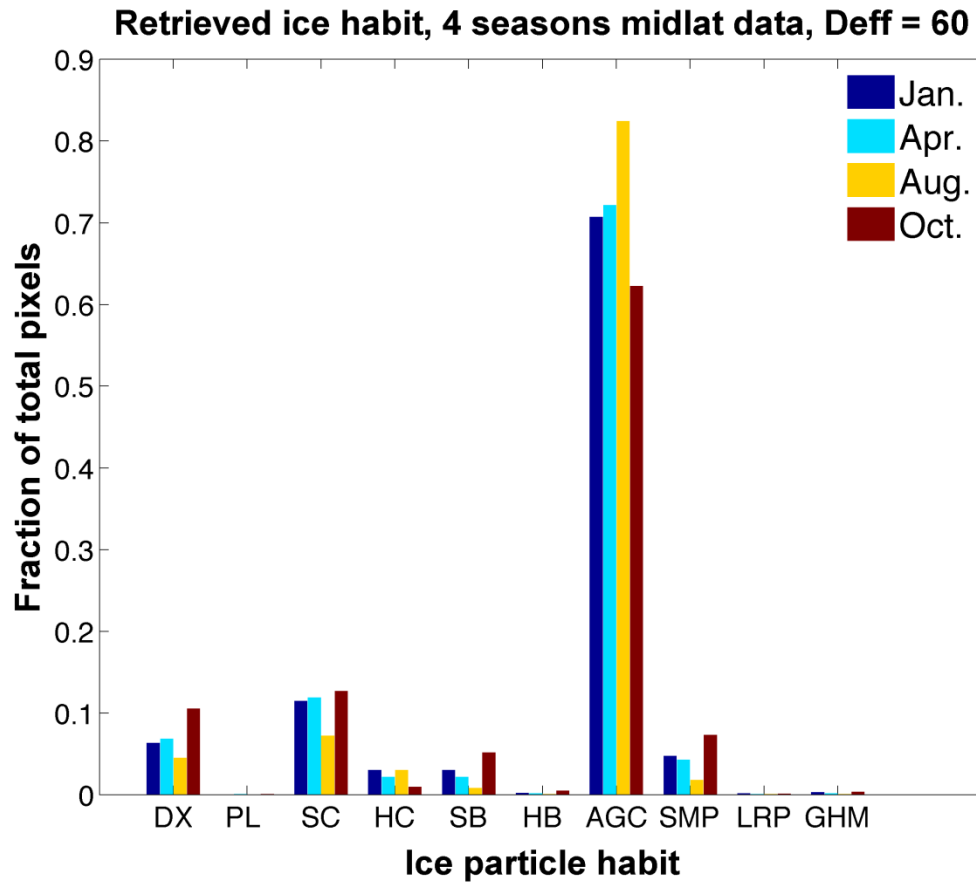
Fig. 19. Ice habit retrieved in midlatitude regions. This shows a histogram of the fraction of total pixels retrieved as one of the 9 single habits or habit mixture, shown for data from 4 different months in midlatitude regions only. DX = droxtal, PL = plate, SC = solid column, HC = hollow column, SB = solid bullet rosette, HB = hollow bullet rosette, AGC = compact aggregate of columns, SMP = 5 member spatial aggregate of plates, LRP = 10-member spatial aggregate of plates, and GHM = General Habit Mix.
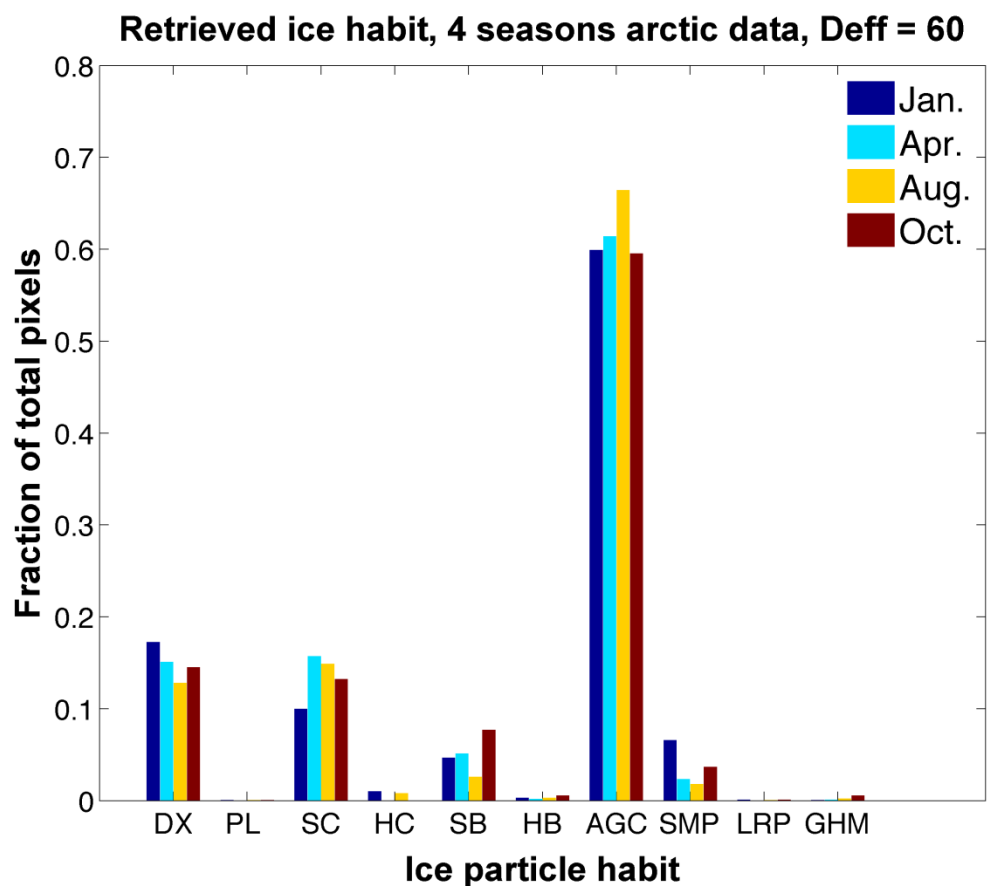
Fig. 20. Ice habit retrieved in polar regions. This shows a histogram of the fraction of total pixels retrieved as one of the 9 single habits or habit mixture, shown for data from 4 different months in polar regions only. DX = droxtal, PL = plate, SC = solid column, HC = hollow column, SB = solid bullet rosette, HB = hollow bullet rosette, AGC = compact aggregate of columns, SMP = 5 member spatial aggregate of plates, LRP = 10-member spatial aggregate of plates, and GHM = General Habit Mix.
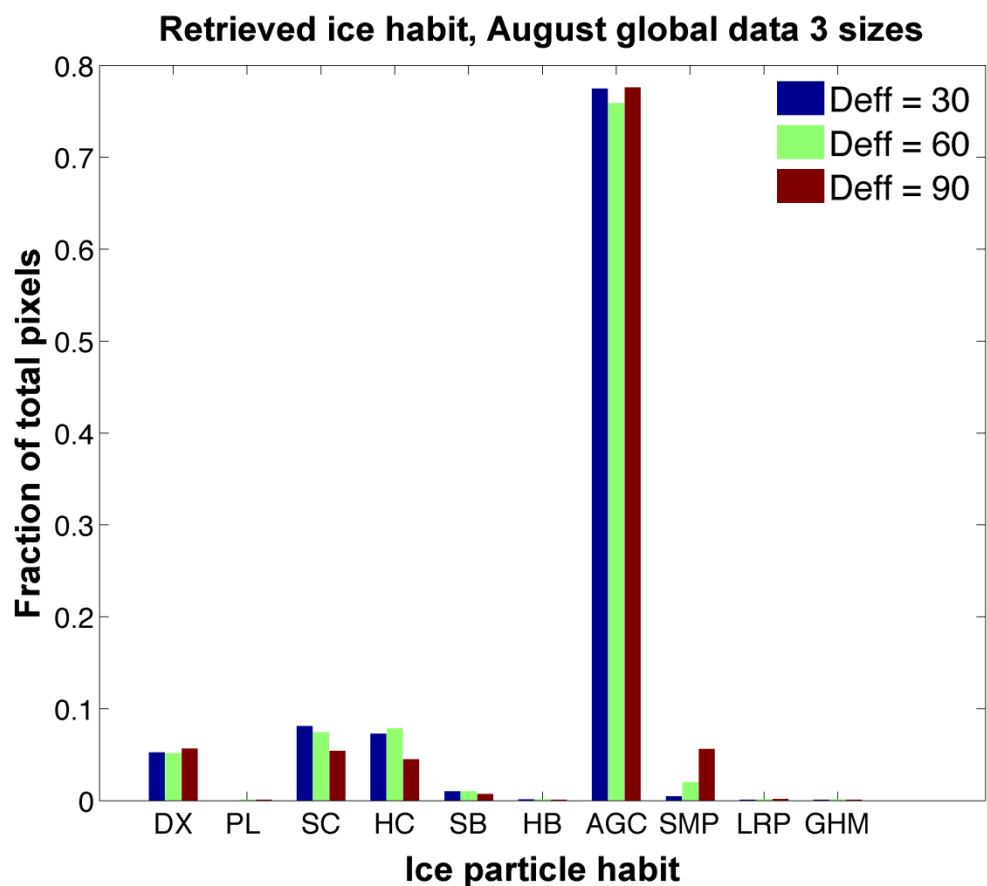
Fig. 21. Retrieved ice habit for 3 effective diameters and data from 1 Aug. 2007. This shows a histogram of the fraction of total pixels retrieved as one of the 9 single habits or habit mixture, shown for 3 different effective diameters and data from 1 August 2007 over the entire globe. DX = droxtal, PL = plate, SC = solid column, HC = hollow column, SB = solid bullet rosette, HB = hollow bullet rosette, AGC = compact aggregate of columns, SMP = 5 member spatial aggregate of plates, LRP = 10-member spatial aggregate of plates, and GHM = General Habit Mix.
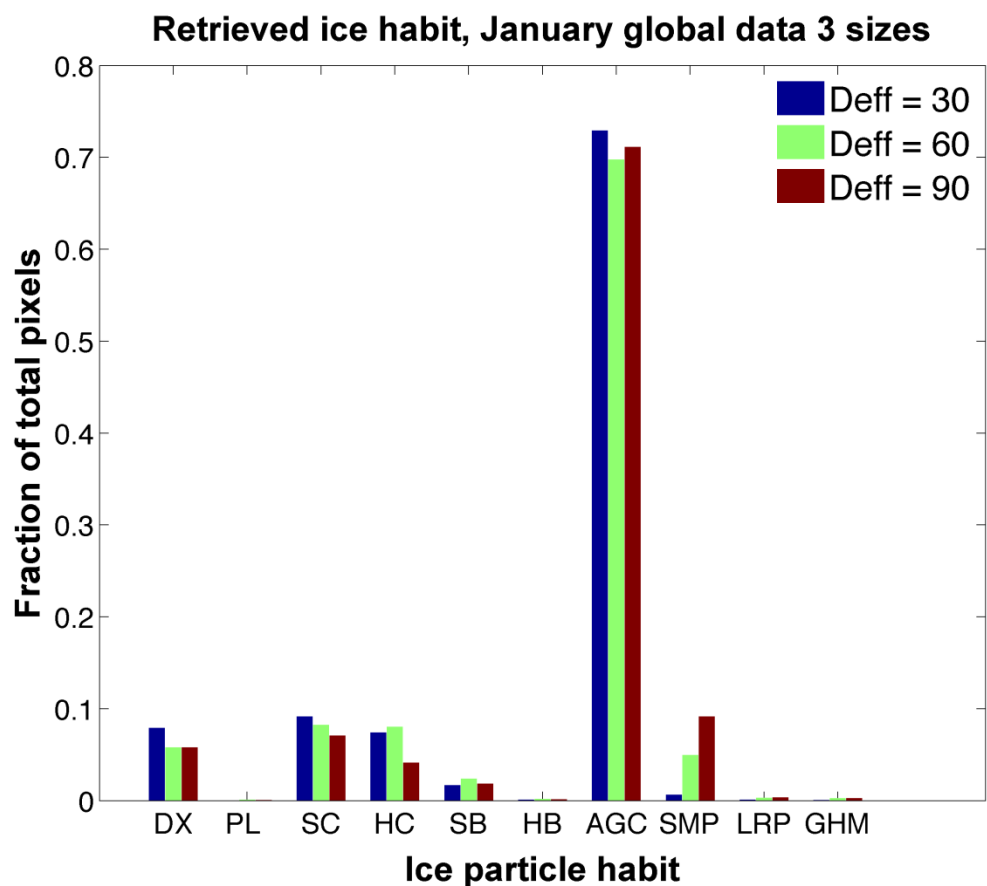
Fig. 22. Retrieved ice habit for 3 effective diameters and data from 1 Jan. 2007. This shows a histogram of the fraction of total pixels retrieved as one of the 9 single habits or habit mixture, shown for 3 different effective diameters and data from 1 January 2007 over the entire globe. DX = droxtal, PL = plate, SC = solid column, HC = hollow column, SB = solid bullet rosette, HB = hollow bullet rosette, AGC = compact aggregate of columns, SMP = 5 member spatial aggregate of plates, LRP = 10-member spatial aggregate of plates, and GHM = General Habit Mix.

Turning to ice roughness now, the global retrieval of ice roughness for an effective diameter of 60 μm is presented in Fig. 23. About 20-30% of pixels return as smooth (i.e., no ice surface roughness present), with the rest having a distribution centered near a roughness value of σ = 0.2, although another peak is present at σ = 0.5. The data from August have the fewest pixels retrieved as smooth with 20%, whereas October has the most at nearly 35%.

Significant differences are seen when separating results for ice roughness by latitude. Pixels in the tropics as seen in Fig. 24 are smooth 5-10% of the time depending on month, and a large fraction of pixels (25% − 40%) are retrieved at a roughness value of σ = 0.5. The same distribution of roughness is seen at smaller roughness values, though the center shifts toward higher roughness at σ = 0.25.

When roughness at midlatitudes is considered as shown in Fig. 25, the distribution of roughness shifts down again to σ = 0.15, and 20-40% of pixels return as smooth. The fraction of smooth pixels varies considerably between August and October, which could indicate these change during different times of the year, or could simply mean that the fraction of smooth pixels varies for other unknown reasons. The ice roughness in polar regions as seen in Fig. 26 again has a distribution centered near σ = 0.15, but even more pixels retrieve as smooth, from 35-45% of the total.
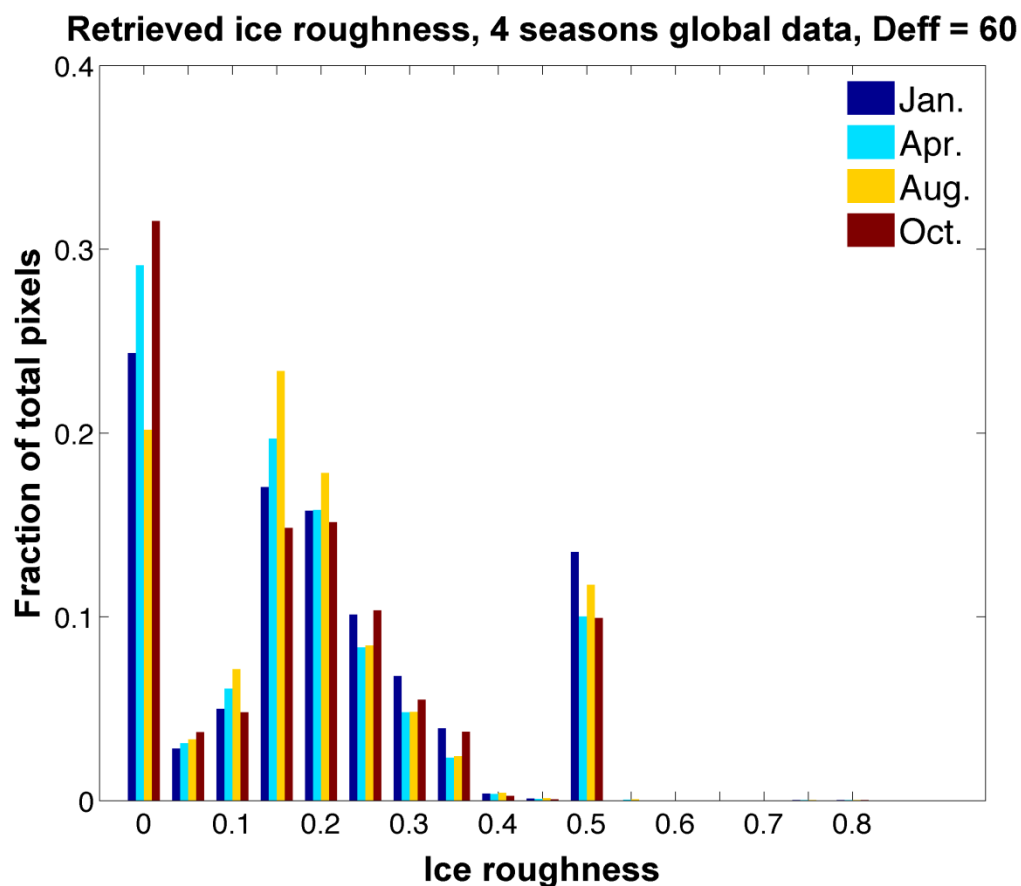
Fig. 23. Global retrieved ice roughness. This shows a histogram of the fraction of total pixels retrieved as one of the 17 values of roughness considered in the retrieval, for global data. σ is a parameter describing the level of surface roughening, with 0 being smooth and 0.8 being extremely rough. DX = droxtal, PL = plate, SC = solid column, HC = hollow column, SB = solid bullet rosette, HB = hollow bullet rosette, AGC = compact aggregate of columns, SMP = 5 member spatial aggregate of plates, LRP = 10-member spatial aggregate of plates, and GHM = General Habit Mix.
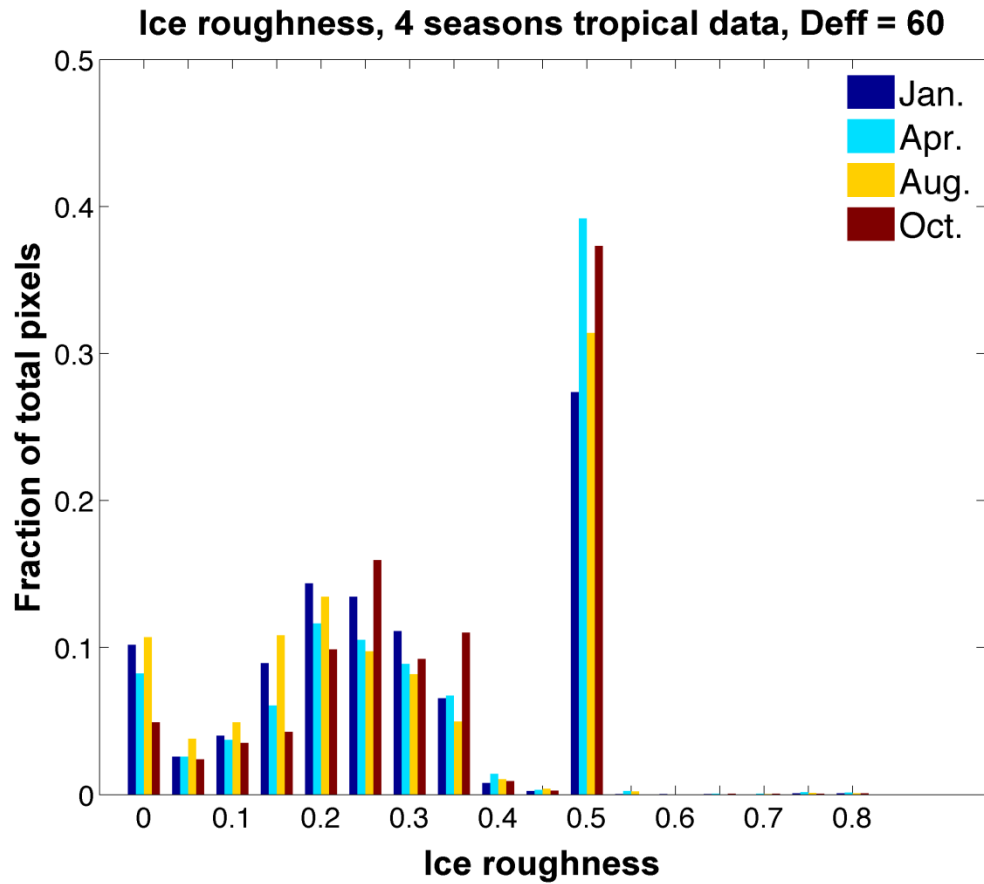
Fig. 24. Ice roughness retrieved in tropical regions. This shows a histogram of the fraction of total pixels retrieved as one of the 17 values of roughness considered in the retrieval, for data from the tropics only. σ is a parameter describing the level of surface roughening, with 0 being smooth and 0.8 being extremely rough. DX = droxtal, PL = plate, SC = solid column, HC = hollow column, SB = solid bullet rosette, HB = hollow bullet rosette, AGC = compact aggregate of columns, SMP = 5 member spatial aggregate of plates, LRP = 10-member spatial aggregate of plates, and GHM = General Habit Mix.
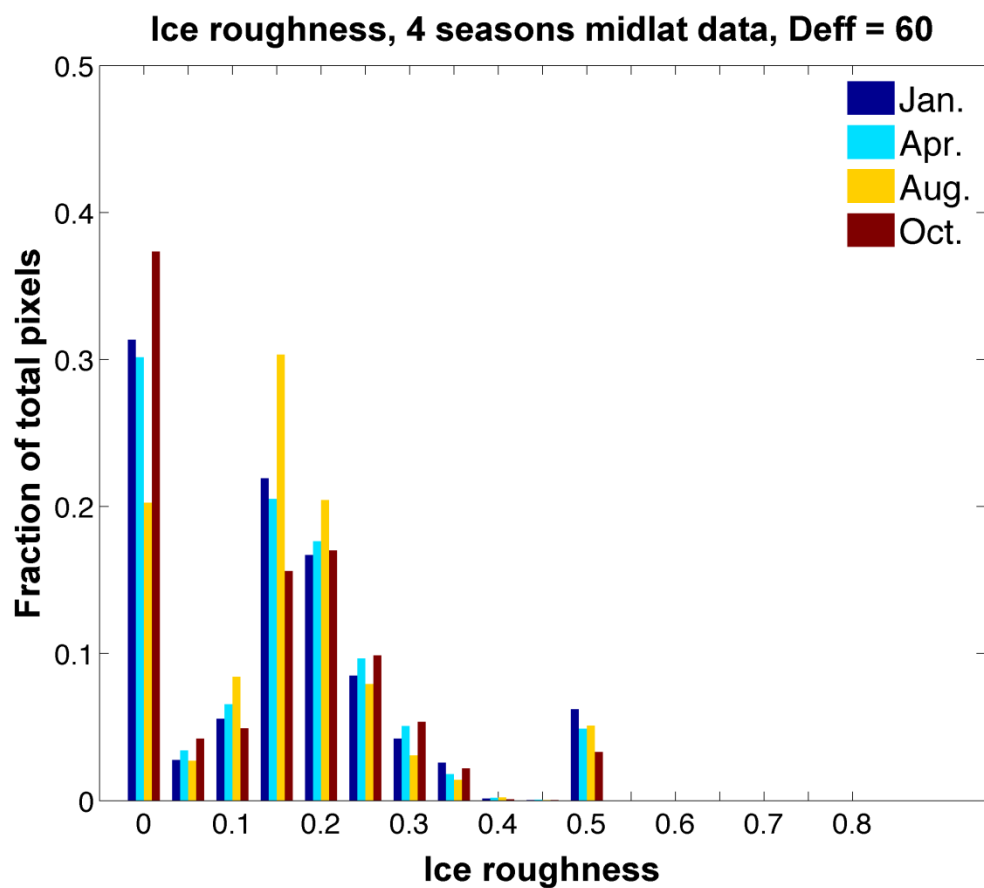
Fig. 25. Ice roughness retrieved in midlatitude regions. This shows a histogram of the fraction of total pixels retrieved as one of the 17 values of roughness considered in the retrieval, for midlatitude data. σ is a parameter describing the level of surface roughening, with 0 being smooth and 0.8 being extremely rough. DX = droxtal, PL = plate, SC = solid column, HC = hollow column, SB = solid bullet rosette, HB = hollow bullet rosette, AGC = compact aggregate of columns, SMP = 5 member spatial aggregate of plates, LRP = 10-member spatial aggregate of plates, and GHM = General Habit Mix.
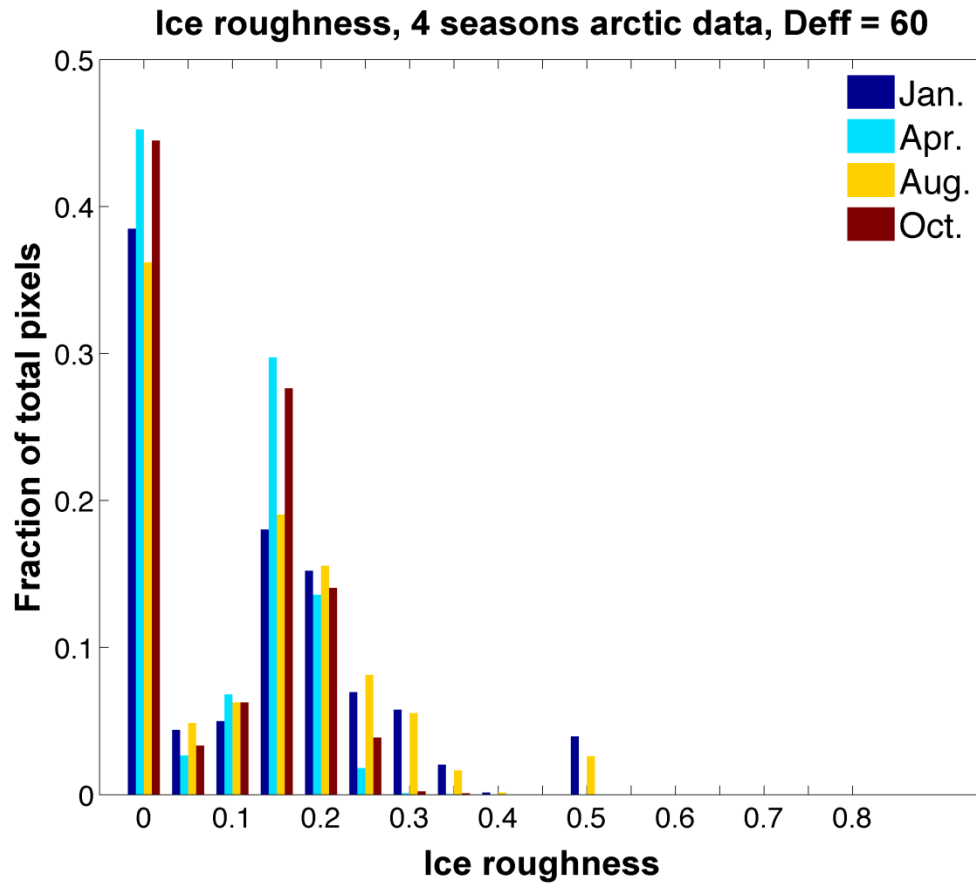
Fig. 26. Ice roughness retrieved in polar regions. This shows a histogram of the fraction of total pixels retrieved as one of the 17 values of roughness considered in the retrieval, for data from polar regions. σ is a parameter describing the level of surface roughening, with 0 being smooth and 0.8 being extremely rough. DX = droxtal, PL = plate, SC = solid column, HC = hollow column, SB = solid bullet rosette, HB = hollow bullet rosette, AGC = compact aggregate of columns, SMP = 5 member spatial aggregate of plates, LRP = 10-member spatial aggregate of plates, and GHM = General Habit Mix.

Retrieved ice roughness has more of a dependence on the ice effective diameter. For PARASOL data from 1 August 2007, Fig. 27 indicates that especially at roughness value of $\sigma = 0.5$, changing the effective diameter from 30 μm to 90 μm decreases the fraction of pixels that will be retrieved at that roughness value and shifts these retrievals to lower roughness. For 1 January 2007 PARASOL data, the retrieval shows the same shifting of roughness, as Fig. 28 demonstrates. Increasing the effective size decreases the roughness for $\sigma = 0.5$ and shifts the distribution of roughness lower.

To examine what habits are retrieved if the roughness is retrieved as smooth, Fig. 29 shows a histogram of the retrieved habit for these pixels. Three effective diameters are shown, and the PARASOL data is from 1 August 2007. In contrast to the retrievals of habit for all data, if roughness is retrieved as smooth, the aggregate of columns is just 40-50% of the total. Solid columns see a substantial increase and make up 25-40% of the retrievals, and droxtals, solid 3D bullet rosettes, and a 5-member aggregate of plates make up the rest. Fig. 30 shows a histogram of retrieved habit for pixels whose roughness is retrieved as very rough, or a σ value of 0.5. Only two habits have a non-negligible appearance, hollow columns and the compact aggregate of columns. Results vary based on effective diameter, but in general the aggregate of columns is retrieved slightly more often for very rough pixels. The same patterns for smooth and rough pixels are seen if PARASOL data from other months of the year is used in the analysis.
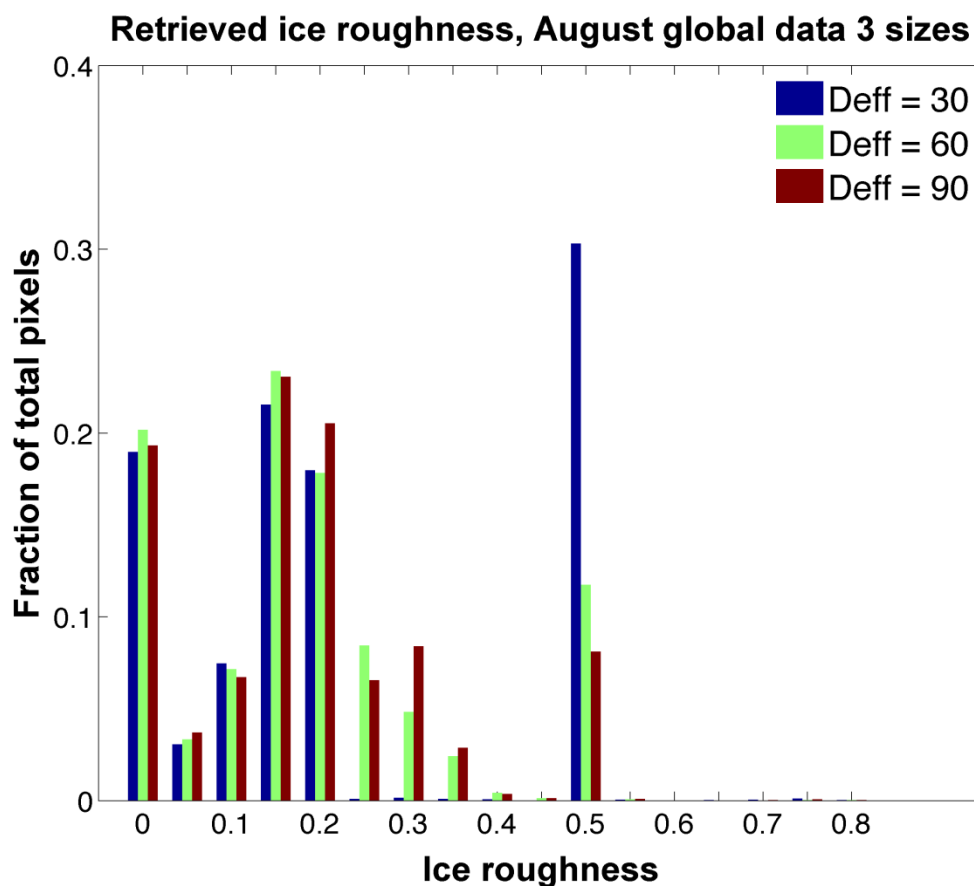
Fig. 27. Ice roughness for 3 effective diameters and data from 1 Aug. 2007. This shows a histogram of the fraction of total pixels retrieved as one of the 17 values of roughness considered in the retrieval, for 3 ice effective diameters and global data from 1 August 2007. σ is a parameter describing the level of surface roughening, with 0 being smooth and 0.8 being extremely rough. DX = droxtal, PL = plate, SC = solid column, HC = hollow column, SB = solid bullet rosette, HB = hollow bullet rosette, AGC = compact aggregate of columns, SMP = 5 member spatial aggregate of plates, LRP = 10-member spatial aggregate of plates, and GHM = General Habit Mix.
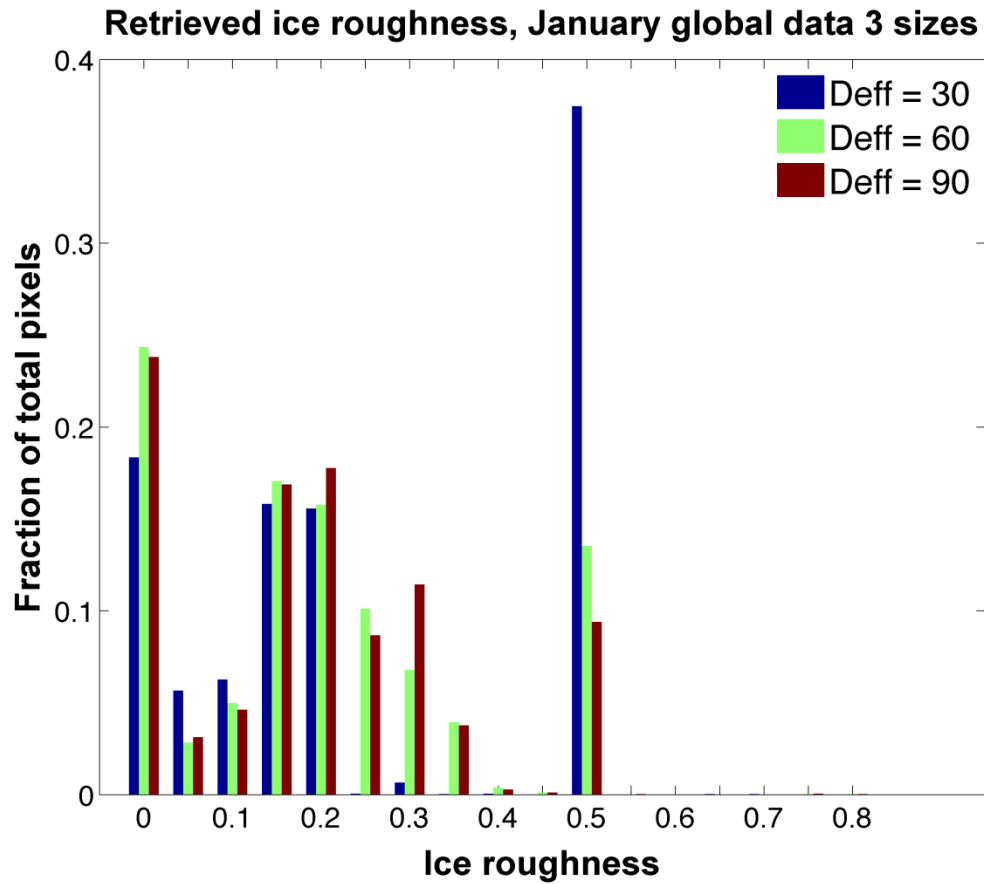
Fig. 28. Ice roughness for 3 effective diameters and data from 1 Jan. 2007. This shows a histogram of the fraction of total pixels retrieved as one of the 17 values of roughness considered in the retrieval, for 3 ice effective diameters and global data from 1 January 2007. σ is a parameter describing the level of surface roughening, with 0 being smooth and 0.8 being extremely rough. DX = droxtal, PL = plate, SC = solid column, HC = hollow column, SB = solid bullet rosette, HB = hollow bullet rosette, AGC = compact aggregate of columns, SMP = 5 member spatial aggregate of plates, LRP = 10-member spatial aggregate of plates, and GHM = General Habit Mix.

Fig. 29. Ice habit retrieved for smooth surfaced ice. This shows a histogram of the fraction of total pixels retrieved as one of the 9 single habits or habit mixture, shown here only for pixels retrieved as smooth and 3 effective diameters. DX = droxtal, PL = plate, SC = solid column, HC = hollow column, SB = solid bullet rosette, HB = hollow bullet rosette, AGC = compact aggregate of columns, SMP = 5 member spatial aggregate of plates, LRP = 10-member spatial aggregate of plates, and GHM = General Habit Mix.
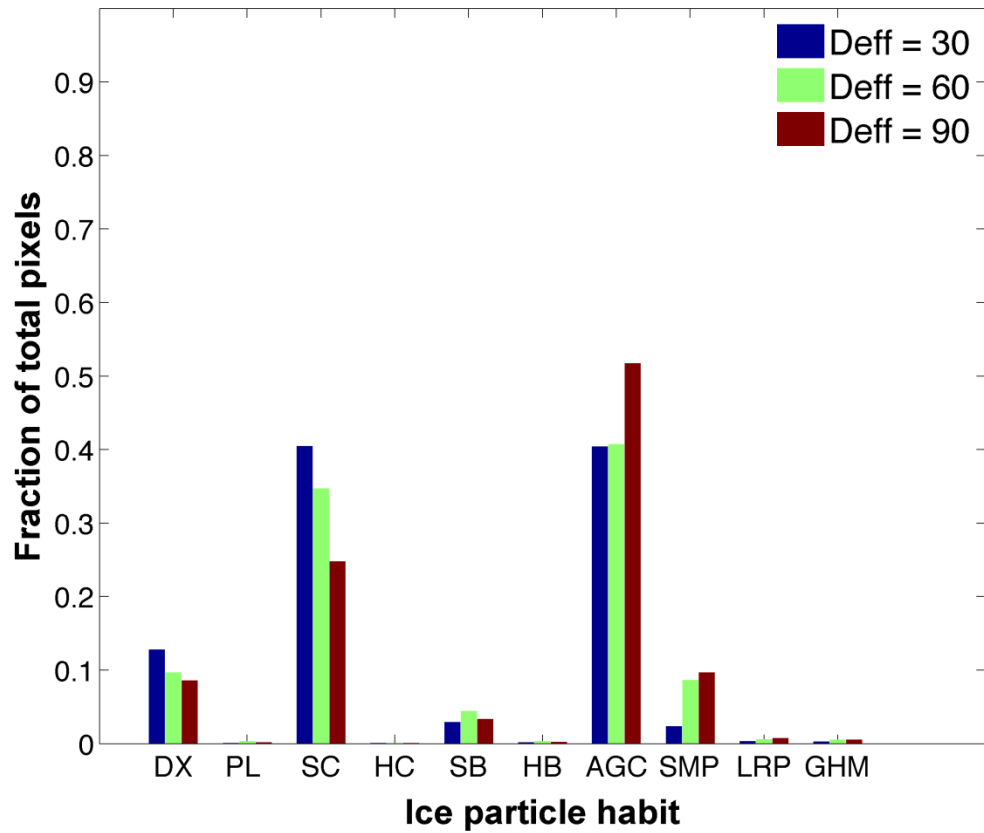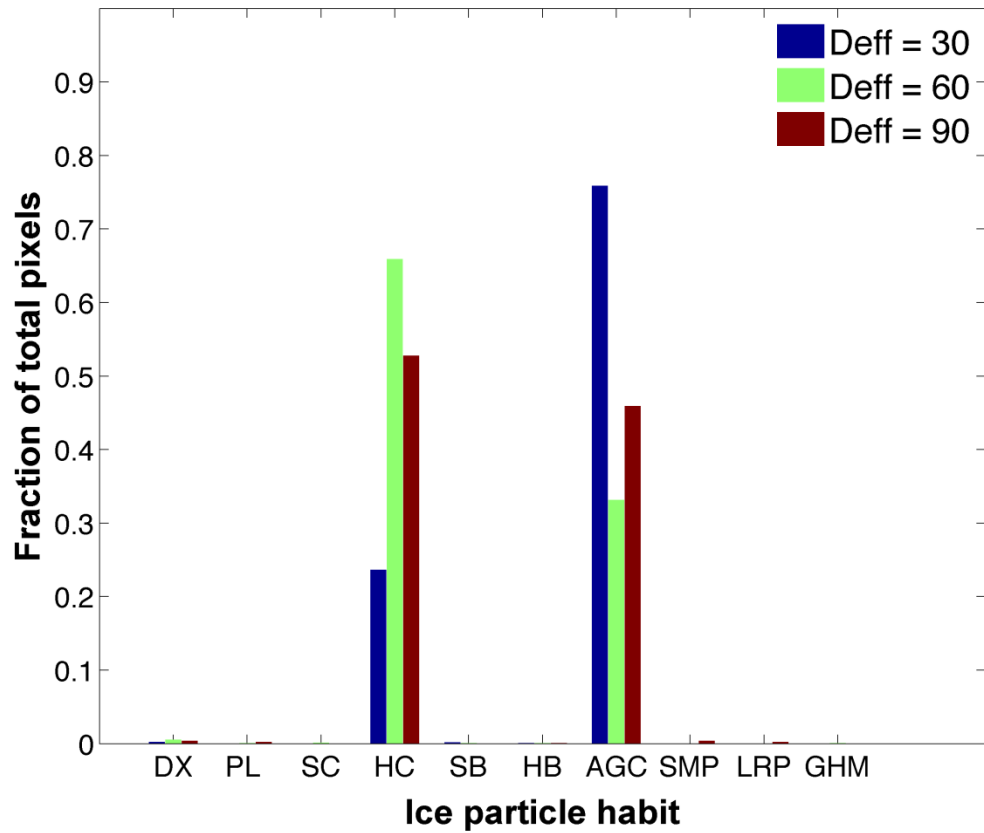
Fig. 30. Ice habit retrieved for rough surfaced ice. This shows a histogram of the fraction of total pixels retrieved as one of the 9 single habits or habit mixture, shown for pixels retrieved as very rough (σ=0.5) and 3 effective diameters. DX = droxtal, PL = plate, SC = solid column, HC = hollow column, SB = solid bullet rosette, HB = hollow bullet rosette, AGC = compact aggregate of columns, SMP = 5 member spatial aggregate of plates, LRP = 10-member spatial aggregate of plates, and GHM = General Habit Mix.

No single habit and roughness combination can reproduce polarized reflectance seen from PARASOL observations, as the previous results show, but the aggregate of columns would represent a large fraction of pixels, and a roughness value of $\sigma = 0.2$ is near the median of the distribution of roughness. Fig. 31 shows the polarized reflectance of this ice habit and roughness. At large scattering angles it appears to be an excellent fit to PARASOL measured on 1 August 2007, but not at small scattering angles. However, a majority of the PARASOL measurements fall in the scattering angle range where this ice habit fits the best.

To investigate the scattering properties of this ice shape further, Fig. 32 shows the full single-scattering phase matrix of the aggregate of columns at three different roughness values. Adding roughness will change all the elements of the phase matrix, but the ones most important for remote sensing are P11 and P12/P11, shown in the two left side panels. The top left panel shows P11, the scattering phase function. Numerous peaks exist at halo angles for the smooth ice which disappear as the roughness value increases. The element P12/P11 shown in the bottom left panel represents the linear polarization and clearly shows that there are oscillatory features seen there which are also represented in the multiple-scattering polarized reflectance results calculated from the adding-doubling radiative transfer model. Adding roughness removes these features and results in a nearly featureless linear polarization curve.
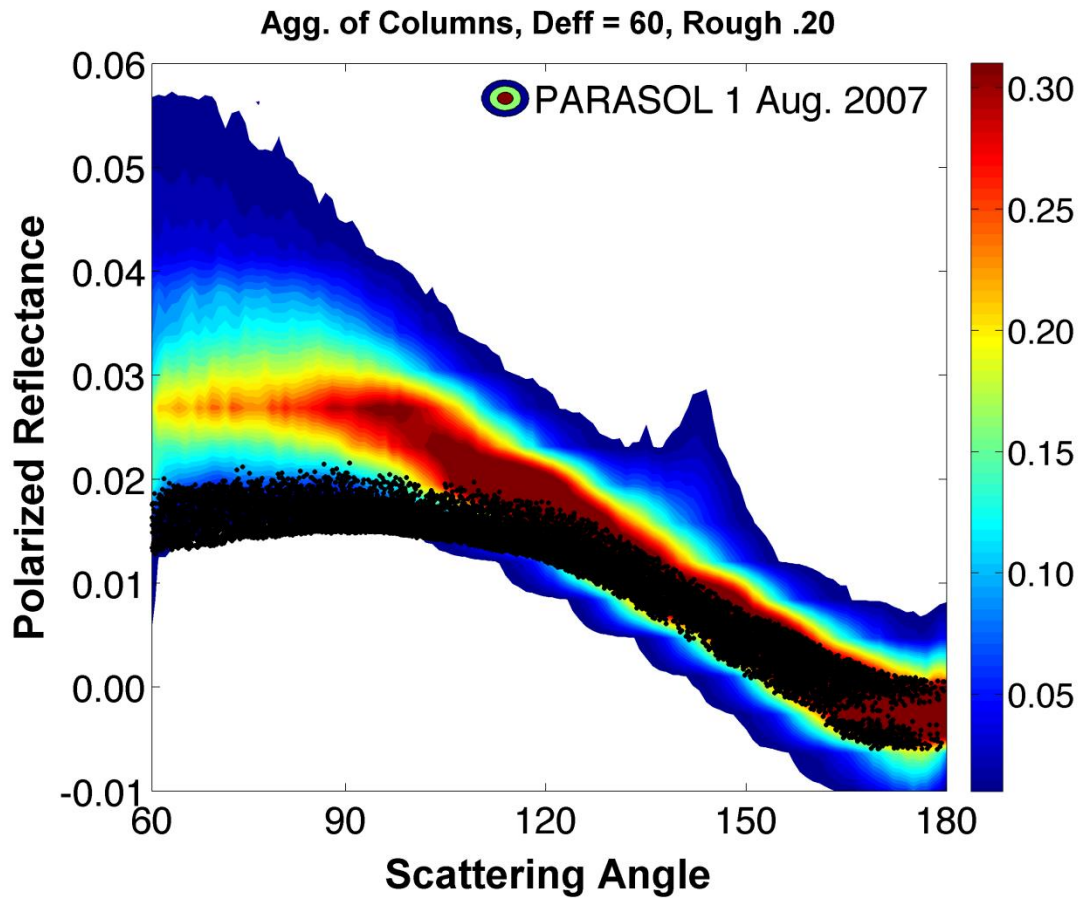
Fig. 31. Polarized reflectance simulated for a compact aggregate of columns. The effective diameter is 60 μm and the roughness value is σ = 0.2. Ice cloud optical thickness is 5. Color contours are density of PARASOL polarized reflectance observations, and black dots are simulations. Each dot represents a calculation of polarized reflectance for a single viewing geometry.
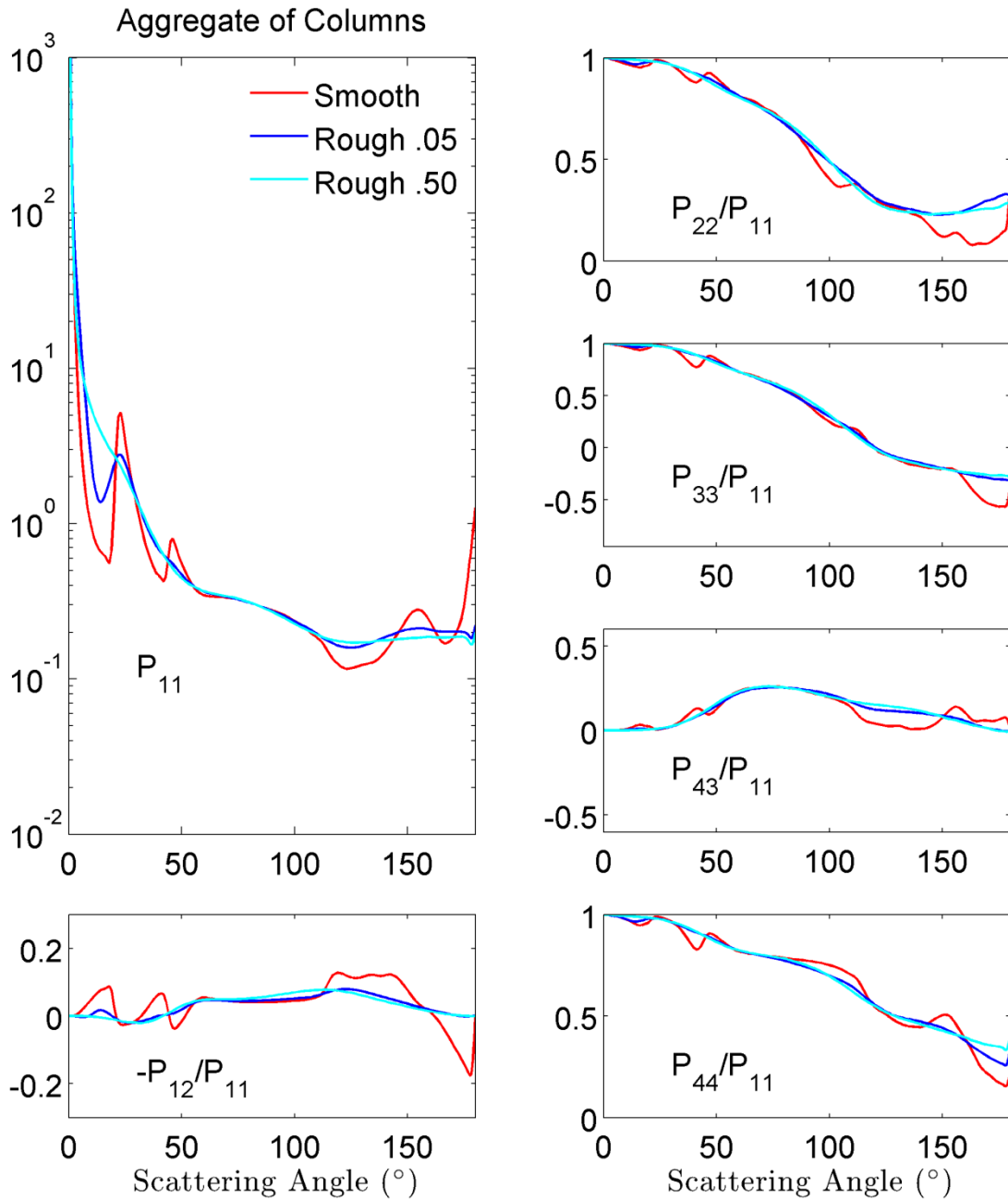
Fig. 32. Single-scattering phase matrix for a compact aggregate of columns. This assumes three different levels of surface roughness. The phase function P11 is shown in the top left panel, while the degree of linear polarization –P12/P11 is shown in the bottom left panel.

84

The results of the retrieval algorithm for the mean and median ice roughness are summarized in Table 3. The mean retrieved roughness varies between a σ value of 0.15 and 0.25, while the median roughness is consistently a σ value of 0.15 or 0.2. Mean retrieved roughness is larger if a smaller ice effective diameter is assumed in simulations, while the median roughness is the same for all four months of data no matter which effective diameter is used in simulations.

Upon retrieving the ice particle roughness and habit and assuming an effective diameter, the ice asymmetry parameter g can be found from single-scattering calculations (described in Chapter III). The asymmetry parameter is a measure of the relative amounts of forward and backward scattering, with complete forward scattering represented by a g value of 1 and lower values indicating more backscattering. Table 4 provides values for the retrieved asymmetry parameter for all four days of data and three effective diameters. Mean values for all cases are near 0.77, while median values are slightly lower near 0.75. The mean asymmetry parameter increases if the assumed effective diameter increases, while the median value decreases slightly.

Table 3. Mean and median retrieved ice roughness for all four days of data and three effective diameter sizes.

Month	January	April	August	October
Deff = 30 μm	Mean: 0.25 Median: 0.2	Mean: 0.2 Median: 0.15	Mean: 0.25 Median: 0.15	Mean: 0.25 Median: 0.15
Deff = 60 μm	Mean: 0.2 Median: 0.2	Mean: 0.15 Median: 0.15	Mean: 0.2 Median: 0.15	Mean: 0.15 Median: 0.15
Deff = 90 μm	Mean: 0.2 Median: 0.2	Mean: 0.15 Median: 0.15	Mean: 0.2 Median: 0.15	Mean: 0.15 Median: 0.15

Table 4. Retrieved values of the asymmetry parameter *g* for all four months of data and three effective diameter sizes considered.

Month	January	April	August	October
Deff = 30 μm	Mean = 0.7626 Median = 0.7538	Mean = 0.7632 Median = 0.7538	Mean = 0.7602 Median = 0.7538	Mean = 0.7650 Median = 0.7538
Deff = 60 μm	Mean = 0.7695 Median = 0.7492	Mean = 0.7695 Median = 0.7492	Mean = 0.7639 Median = 0.7491	Mean = 0.7737 Median = 0.7508
Deff = 90 μm	Mean = 0.7713 Median = 0.7498	Mean = 0.7711 Median = 0.7498	Mean = 0.7652 Median = 0.7496	Mean = 0.7758 Median = 0.7498

CHAPTER VII

SUMMARY AND CONCLUSIONS

In this study an adding-doubling radiative transfer model was used to simulate the polarized reflectance observed at the top of the atmosphere for ten different ice habits and 17 different roughness values. These simulations were performed for the entire range of viewing geometries observed by the PARASOL instrument, and the results were stored in a lookup table for use in a retrieval algorithm.

Simulated polarized reflectance for several ice shapes and levels of roughness was first examined to see how roughness can change the qualitative fit to polarized reflectance. As expected from previous results (Baran; C.-Labonnote 2007; C.-Labonnote et al. 2001; Cole et al. 2013), smooth ice cannot match the observed polarized reflectance over the entire range of scattering angles. Introduction of surface roughness evens out the simulated polarized reflectance and lowers its magnitude. As the surface roughness increases to the maximum considered value of $\sigma = 0.8$, polarized reflectance changes very little except at scattering angles below 120 degrees where it increases slightly.

Retrievals of ice particle shape and roughness from satellite measurements of polarized reflectance were done by minimizing the differences between simulated polarized reflectance and the PARASOL measurements at the viewing geometries for each PARASOL pixel. Retrievals were done for 4 days of global data from 4 different months of the year. Each day of data contained between 50,000 and 70,000 pixels.

Considering retrievals incorporating global data, the ice habit which was retrieved most often in all cases was the compact aggregate of columns. Retrieved fractions were generally between 60% and 70% for the compact aggregate of columns, and various other shapes contributed small amounts. If the data is separated by latitude, the compact aggregate of columns is still the most often retrieved habit.

Considering global data, some level of roughness was retrieved in approximately 70% of pixels and did not vary considerably month to month. The mean retrieved roughness was a σ value of 0.2, corresponding to a value in between "moderate" and "severe" surface roughness values (0.03,0.50) seen in the literature (Cole et al. 2013; Yang et al. 2008).

Retrieved roughness varies considerably depending on latitude. If PARASOL data from only the tropics (30N – 30S) is considered, smooth ice particles are retrieved for only 5-10% of cases, depending on month. Very rough ice of σ = 0.5 is retrieved in approximately 30-40% of cases. For midlatitude data, smooth ice is 20-40% of retrieved pixels, and for polar regions it is as much as 45%.

The small amount of smooth ice in the tropics may be due to different processes generating the ice clouds seen there. Deep convection dominates the tropics and blowoff from this convection forms many of the ice clouds seen by satellite (Baran 2009) In-situ studies have found aggregates are common in deep convective ice clouds (Um; McFarquhar 2007), and the efficient riming processes within the thunderstorm anvil may be contributing to the surface roughness measured for pixels in the tropics (Baran et al. 2011).

Ice clouds in the midlatitudes and polar regions are generated more often by synoptic processes, where mixed-phase riming would be less likely and the ice forms at colder temperatures. Smooth ice tends to form when the temperature is very low (Magono; Lee 1966).

The retrieved habit does not depend on the ice effective diameter used in the simulations, which is expected since polarization has little dependence on the ice particle size. However, the retrieved roughness does have some dependence on ice size, especially for larger values of roughness. This points to the need for a retrieval algorithm incorporating infrared wavelengths to determine the ice particle effective diameter before proceeding with a retrieval of roughness using polarization. However, because the dependence is not strong, retrievals using an average value for ice effective diameter should not have large errors in retrieved roughness.

The polarized reflectance plotted against density of PARASOL measurements for the most commonly retrieved shape and roughness of a compact aggregate of columns and roughness of $\sigma = 0.2$ matches very well except for small scattering angles. This could be caused by the presence of smooth ice crystals and rough ice crystals in the same PARASOL scene, since smooth ice tends to have higher polarization at small scattering angles. No mixtures of rough ice and smooth ice were used in the retrieval, however. The retrieval method selects the single level of roughness describing the entire population of ice crystals in the cloud which fits the best with measured polarized reflectances.

Various field campaigns have noted that aggregates are a very common ice habit, especially near deep convection (Baran et al. 2011; Garrett et al. 2005). Van Diedenhoven et al. (2012) found that ice which had a very low asymmetry parameter and high distortion best matched measurements from the Research Scanning Polarimeter (Cairns et al. 2003) instrument. Collocated in-situ probes indicated a high level of aggregate ice particles, indicating a low asymmetry parameter below 0.8.

The compact aggregate of columns has the lowest asymmetry parameter values of any ice habit among the 10 habits and mixtures considered in the present study. Because aggregates were the most commonly retrieved habit, the retrieved asymmetry parameter should also be low. The asymmetry parameter for all data considered had a mean value near 0.77 for all months, with a median value closer to 0.75. Van Diedenhoven et al. (2013) reported retrieved asymmetry parameter values of between 0.76 and 0.8 with a median value of 0.78, so the asymmetry parameter retrieved in this study is slightly lower but still comparable. However, other results in the literature report asymmetry parameters of about 0.73, slightly lower than the values from the present retrieval (Gerber et al. 2000).

It is important to note that the surface roughness in the present model cannot be related to any physical size, and as such it is difficult to compare the retrieved roughness to in-situ measurements of ice roughness. These retrieval results can, however, serve as a guide for ice model development with the goal of reducing uncertainties in the description of the radiative properties of ice clouds.

This work may be further extended by producing year-long and multi-year climatologies of the retrieved habit, roughness, and asymmetry parameter from PARASOL polarized reflectance measurements. RSP measurements of polarized reflectance can be used in the future using the same method (van Diedenhoven et al. 2013).

Ice habit and roughness have a significant impact on the radiative properties of ice clouds, so it is necessary to describe these parameters accurately when doing global modeling or satellite retrievals. For ice cloudy scenes specifically in the midlatitudes or polar regions, different ice models incorporating more smooth ice and more pristine ice habits may represent the microphysics better. When using only one ice habit, however, an aggregate of columns with a lower roughness value or even smooth surfaces may be the best model to use in these regions. For tropical regions, higher values of roughness are generally retrieved and therefore must be incorporated into model simulations. Based on the results of this study, an ice model which captures the microphysics on a global scale of the large majority of ice cloudy scenes observed by PARASOL is the compact aggregate of columns with a roughness value of $\sigma = 0.20$.

REFERENCES

Adams, C. N., and G. W. Kattawar, 1993: Effect of volume scattering function on the errors induced when polarization is neglected in radiance calculations in an atmosphere-ocean system. *Appl. Opt.*, **32,** 4610-4617.

Baran, A. J., 2009: A review of the light scattering properties of cirrus. *J. Quant. Spectrosc. Radiat. Transfer*, **110,** 1239-1260.

Baran, A.J., 2012: From the single-scattering properties of ice crystals to climate prediction: A way forward. *Atmos. Res.* , **112,** 45-69.

Baran, A. J., and L. C.-Labonnote, 2006: On the reflection and polarization properties of ice cloud. *J. Quant. Spectrosc. Radiat. Transfer*, **100,** 41-54.

Baran, A.J., 2007: A self-consistent scattering model for cirrus. I: the solar region. *Q.J. Roy. Meteor. Soc.* , **133,** 1899-1912.

Baran, A. J., P. J. Connolly, A. J. Heymsfield, and A. Bansemer, 2011: Using in situ estimates of ice water content, volume extinction coefficient, and the total solar optical depth obtained during the tropical ACTIVE campaign to test an ensemble model of cirrus ice crystals. *Q.J. Roy. Meteor. Soc.*, **137,** 199-218.

Baum, B. A., P. Yang, Y. X. Hu, and Q. Feng, 2010: The impact of ice particle roughness on the scattering phase matrix. *J. Quant. Spectrosc. Radiat. Transfer*, **111,** 2534-2549.

Baum, B. A., P. Yang, A. J. Heymsfield, S. E. Platnick, M. D. King, Y. X. Hu, and S. T. Bedka, 2005: Bulk scattering properties for the remote sensing of ice clouds. part II: narrowband models. *J. Appl. Meteor. Climatol.*, **44,** 1896-1911.

Baum, B. A., Yang, P., Heymsfield, A.J., Schmitt, C.G., Xie, Y., et al, 2011: Improvements in shortwave bulk scattering and absorption models for the remote sensing of ice clouds. *J. Appl. Meteor. Climatol.*, **50,** 1037-1056.

Baumgardner, D., H. Chepfer, G. B. Raga, and G. L. Kok, 2005: The shapes of very small cirrus particles derived from in situ measurements. *Geophys. Res. Lett.*, **32,** L01806.

Baumgardner, D., Brenguier, J.L., Bucholtz, A., Coe, H., DeMott, P., et al, 2011: Airborne instruments to measure atmospheric aerosol particles, clouds and radiation: A cook's tour of mature and emerging technology. *Atmos. Res.*, **102,** 10-29.

Bi, L., Yang, P., Kattawar, G.W., Baum, B.A., Hu, Y.X., et al, 2009: Simulation of the color ratio associated with the backscattering of radiation by ice particles at the wavelengths of 0.532 and 1.064 μm. *J. Geophys. Res.* , **114,** D00H08.

Bohren, C. F., and D. R. Huffman, 1983: *Absorption and Scattering of Light by Small Particles.* Wiley, New York.

Breon, F. M., 2006: *Parasol Level-1 Product Data Format and User Manual.* CNES, Paris.

Breon, F.M., 2009: *Parasol Level-2 Product Data Format and User Manual.* CNES, Paris.

C.-Labonnote, L., G. Brogniez, J. C. Buriez, and M. Doutriaux-Boucher, 2001: Polarized light scattering by inhomogeneous hexagonal monocrystals: Validation with ADEOS-POLDER measurements. *J. Geophys. Res.* , **106,** 12,139-153.

Cairns, B., E. E. Russell, J. D. LaVeigne, and P. M. W. Tennant, 2003: Research Scanning Polarimeter and airborne usage for remote sensing of aerosols. *Proc. SPIE*, **5158,** 33-44.

Chami, M., R. Santer, and E. Dilligeard, 2001: Radiative transfer model for the computation of radiance and polarization in an ocean-atmosphere system: polarization properties of suspended matter for remote sensing. *Appl. Opt.*, **40,** 2398-2416.

Chandrasekhar, S., 1947: On the radiative equilibrium of a stellar atmosphere. XV. *Astrophys. J.* , **105,** 424.

Chandrasekhar, S., 1960: *Radiative Transfer.* Dover, New York.

Chepfer, H., G. Brogniez, and Y. Fouquart, 1998: Cirrus clouds' microphysical properties deduced from POLDER observations. *J. Quant. Spectrosc. Radiat. Transfer*, **60,** 375-390.

Cole, B. H., P. Yang, B. A. Baum, J. Riedi, L. C.-Labonnote, F. Thieuleux, and S. E. Platnick, 2013: Comparison of PARASOL observations with polarized reflectances simulated using different ice habit mixtures. *J. Appl. Meteor. Climatol.*, **52,** 186-196.

de Haan, J. F., P. B. Bosma, and J. W. Hovenier, 1987: The adding method for multiple scattering calculations of polarized light. *Astron. Astrophys.*, **183,** 371-391.

Ditchburn, R. W., 1991: *Light.* Dover, New York.

Fougnie, B., G. Bracco, B. Lafrance, C. Ruffel, O. Hagolle, and C. Tinel, 2007: PARASOL in-flight calibration and performance. *Appl. Opt.*, **46,** 5435-5451.

Garrett, T. J., Navarro, B.C., Twohy, C.H., Jensen, E.J., Baumgardner, D.G, et al, 2005: Evolution of a Florida Cirrus Anvil. *J. Atmos. Sci.*, **62,** 2352-2372.

Gayet, J. F., O. Crepel, J. F. Fournol, and S. Oshchepkov, 1997: A new airborne polar Nephelometer for the measurements of optical microphysical cloud properties. Part I: Theoretical design. *Ann. Geophys.*, **15,** 451-459.

Gayet, J. F., G. Mioche, V. Shscherbakov, C. Gourbeyre, R. Buse, and A. Minikin, 2011: Optical properties of pristine ice crystals in mid-latitude cirrus clouds: a case study during CIRCLE-2 experiment. *Atmos. Chem. Phys.*, **11,** 2537-3544.

Gerber, H., Y. Takano, T. J. Garrett, and P. V. Hobbs, 2000: Nephelometer Measurements of the Asymmetry Parameter, Volume Extinction Coefficient, and Backscatter Ratio in Arctic Clouds. *J. Atmos. Sci.*, **57,** 3021-3034.

Guignard, A., C. J. Stubenrauch, A. J. Baran, and R. Armante, 2012: Bulk microphysical properties of semi-transparent cirrus from AIRS: a six year global climatology and statistical analysis in synergy with geometrical profiling data from CloudSat-CALIPSO. *Atmos. Chem. Phys.*, **12,** 503-525.

Hecht, E., 2002: *Optics.* 4th ed. Addison Wesley, San Francisco.

Heymsfield, A. J., and L. M. Miloschevich, 2003: Parameterizations for the Cross-Sectional Area and Extinction of Cirrus and Stratiform Ice Cloud Particles. *J. Atmos. Sci.*, **60,** 936-956.

Hielscher, A. H., A. A. Eick, J. R. Mourant, D. Shen, J. P. Freyer, and I. J. Bigio, 1997: Diffuse backscattering Mueller matrices of highly scattering media. *J. Opt. Soc. Am.*, **1,** 441-453.

Hovenier, J. W., C. Van der Mee, and H. Domke, 2004: *Transfer of Polarized Light in Planetary Atmospheres.* Springer, New York.

Hu, Y. X., B. Wielicki, B. Lin, G. Gibson, S. C. Tsay, K. Stamnes, and T. Wong, 2000: δ-fit: a fast and accurate treatment of particle scattering phase functions with weighted singular-value decomposition least-squares fitting. *J. Quant. Spectrosc. Radiat. Transfer*, **65,** 681-690.

Jackson, J. D., 1998: *Classical Electrodynamics.* 3rd ed. John Wiley and Sons, New York.

Joseph, J. H., W. J. Wiscombe, and J. A. Weinman, 1976: Delta-Eddington approximation for radiative flux-transfer. *J. Atmos. Sci.*, **33,** 2452-2459.

Korolev, A. V., G. A. Isaac, and J. Hallett, 1999: Ice particle habits in Arctic clouds. *Geophys. Res. Lett.*, 1299-1302.

Korolev, A. V., E. F. Emery, J. W. Strapp, S. G. Cober, G. A. Isaac, M. Wasey, and D. Marcotte, 2011: Small Ice Particles in Tropospheric Clouds: Fact or Artifact? *Bull. Amer. Meteor. Soc.*, **92,** 967-973.

Liou, K. N., 1986: Influence of cirrus clouds on weather and climate processes: a global perspective. *Mon. Wea. Rev.*, **114,** 1167-1198.

Liou, K. N., 2002: *An introduction to Atomspheric Radiation.* Academic Press, San Diego.

Mace, G. G., Y. Zhang, S. E. Platnick, M. D. King, P. Minnis, and P. Yang, 2005: Evaluation of Cirrus Cloud Properties Derived from MODIS Data Using Cloud Properties Derived from Ground-Based Observations Collected at the ARM SGP Site. *J. Appl. Meteor. Climatol.*, **44,** 221-240.

Magono, C., and C. W. Lee, 1966: Meteorological Classification of Natural Snow Crystals. *Journal of the Faculty of Science, Hokkaido University*, **II,** 321-335.

Mueller, H., 1948: The foundations of optics. *J. Opt. Soc. Am.*, **38,** 661.

Natraj, V., K. F. Li, and Y. L. Yung, 2009: Rayleigh Scattering in Planetary Atmospheres: Corrected Tables Through Accurate Computation of X and Y Functions. *The Astrophysical Journal*, **69,** 1909-1920.

Nazaryan, H., M. P. McCormick, and W. P. Menzel, 2008: Global characterization of cirrus clouds using CALIPSO data. *J. Geophys. Res.*, **113,** D16211.

Platt, C. M. R., D. W. Reynolds, and N. L. Abshire, 1980: Satellite and Lidar observations of the albedo, emittance and optical depth of cirrus compared to model calculations. *Mon. Wea. Rev.*, **108,** 195-204.

Stephens, G. L., S. C. Tsay, P. W. Stackhouse Jr., and P. J. Flatau, 1990: The relevance of the microphysical and radiative properties of cirrus clouds to climate and climatic feedback. *J. Atmos. Sci.*, **47,** 1742-1754.

Stokes, G. G., 1975: On the composition and resolution of streams of polarized light from different sources. *Polarized Light*, W. Swindell, Ed., Dowden, Hutchinson, and Ross, Stroudsburg, PA, 124-141.

Tomasi, C., V. Vitale, B. Petkov, A. Lupi, and A. Cacciari, 2005: Improved algorithm for calculations of Rayleigh-scattering optical depth in standard atmospheres. *Appl. Optics* **44,** 3320-3341.

Tynes, H. H., G. W. Kattawar, E. P. Zege, I. L. Katsev, and A. S. Prikhach, 2001: Monte Carlo and multicomponent approximation methods for vector radiative transfer by use of effective Mueller matrix calculations. *Appl. Opt.*, **40,** 400-412.

Ulanowski, Z., E. Hesse, P. H. Kaye, and A. J. Baran, 2006: Light scattering by complex ice-analogue crystals. *J. Quant. Spectrosc. Radiat. Trans.*, **100,** 382-392.

Um, J., and G. M. McFarquhar, 2007: Single-scattering properties of aggregates of bullet rosettes in cirrus. . *J. Appl. Meteor. Climatol.*, **46,** 757-775.

van de Hulst, H. C., 1957: *Light Scattering by Small Particles.* John Wiley and Sons, New York.

van de Hulst, H. C., 1980: *Multiple Light Scattering: Tables, Formulas, and Applications.* Vol. Vol. I, Academic Press, San Diego.

van Diedenhoven, B., B. Cairns, A. M. Fridlind, A. S. Ackerman, and T. J. Garrett, 2013: Remote sensing of ice crystal asymmetry parameter using multi-directional polarization measurements - Part 2: Application to the Research Scanning Polarimeter. *Atmos. Chem. Phys.* , **13,** 3185-3203.

van Diedenhoven, B., B. Cairns, I. V. Geogdzhayev, A. M. Fridlind, A. S. Ackerman, P. Yang, and B. A. Baum, 2012: Remote Sensing of ice crystal asymmetry parameter using multi-directional polarization measurements - Part 1: Methodology and evaluation with simulated measurements. *Atmos. Meas. Tech.*, **5,** 2361-2374.

Wiscombe, W. J., 1977: The Delta-M method: rapid yet accurate radiative flux calculations for strongly asymmetric phase functions. *J. Atmo. Sci.* , **34,** 1408-1422.

Yang, P., and K. N. Liou, 1996: Geometric-optics-integral-equation method for light scattering by nonspherical ice crystals. *Appl. Opt.*, **35,** 6568-6584.

Yang, P., and K.N. Liou, 1997: Light scattering by hexagonal ice crystals: solutions by a ray-by-ray integration algorithm. *J. Opt. Soc. Am. A*, **14,** 2278-2289.

Yang, P., and K.N. Liou, 1998: Single-scattering properties of complex ice crystals in terrestrial atmosphere. *Contr. Atmos. Phys.* , **71,** 223-248.

Yang, P., G. W. Kattawar, G. Hong, P. Minnis, and Y. X. Hu, 2008: Uncertainties associated with the surface texture of ice particles in satellite-based retrieval of cirrus clouds: part I. single scattering properties of ice crystals with surface roughness. *IEEE Trans. Geosci. Rem. Sens.* , **46,** 1940-1947.

Yang, P., L. Bi, B. A. Baum, K. N. Liou, G. W. Kattawar, M. Mishchenko, and B. Cole, 2013: Spectrally consistent scattering, absorption, and polarization properties of atmospheric ice crystals at wavelengths from 0.2 μm to 100 μm. *J. Atmos. Sci.*, **70,** 330-347.

Young, A. T., 1980: Revised depolarization corrections for atmospheric extinction. *Appl. Opt.*, **19,** 3427-3428.

Yurkin, M. A., and A. G. Hoekstra, 2011: The discrete-dipole-approximation code ADDA: capabilities and known limitations. *J. Quant. Spectrosc. Radiat. Transfer*, **112,** 2234-2247.
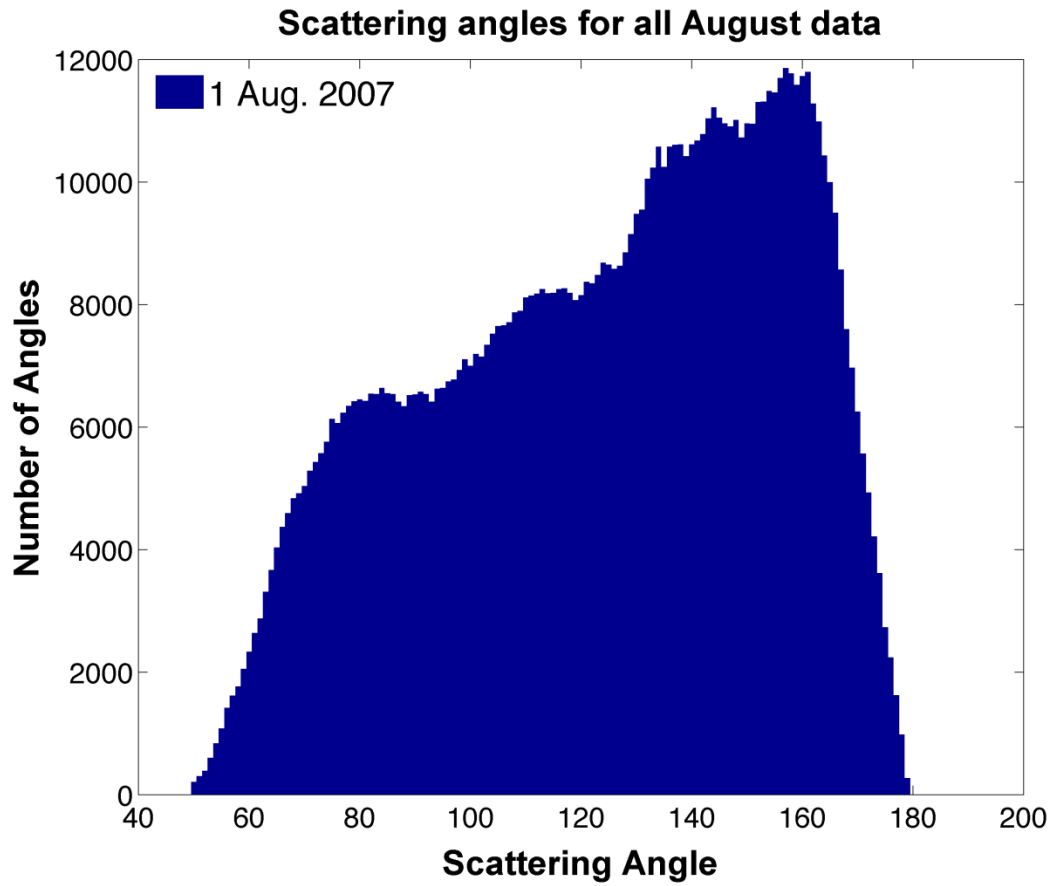
Fig. 33. Histogram of scattering angles from 1 August 2007 data. Much of the data is found at backscattering angles.
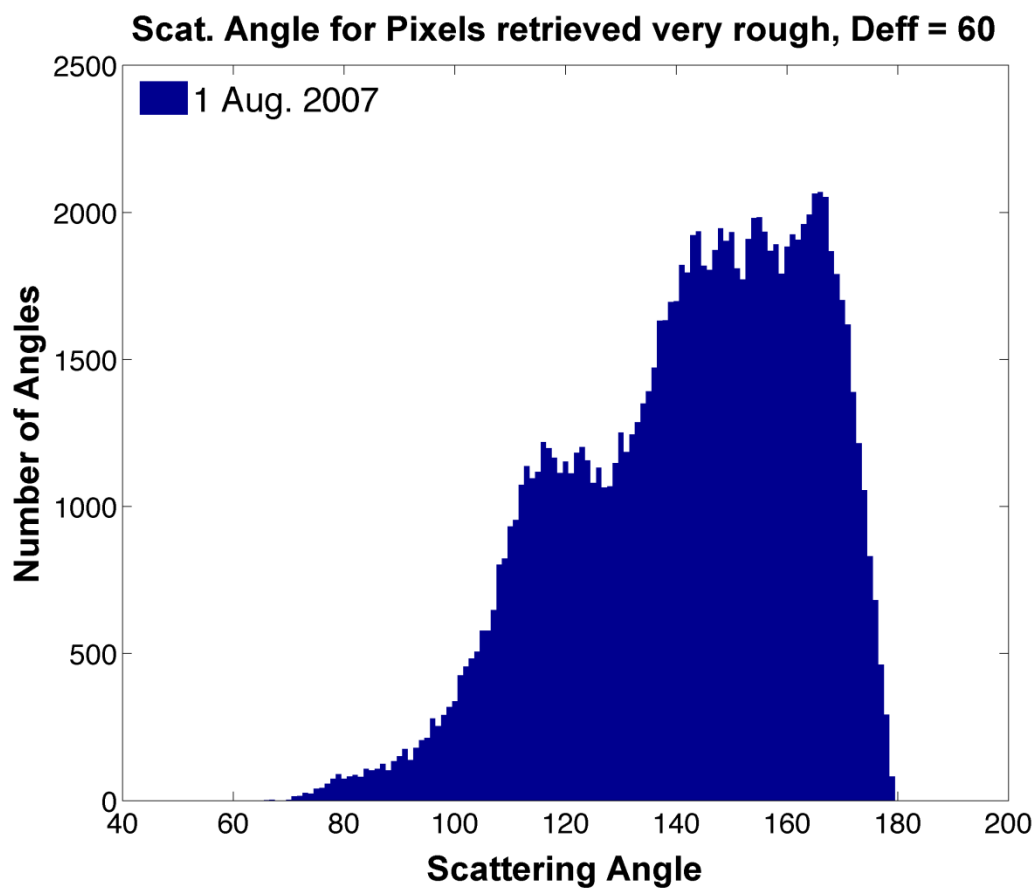
Fig. 34. Histogram of scattering angles for pixels retrieved as very rough. The effective diameter is 60 μm and the PARASOL data is from 1 August 2007. Very rough is a σ value of 0.5.
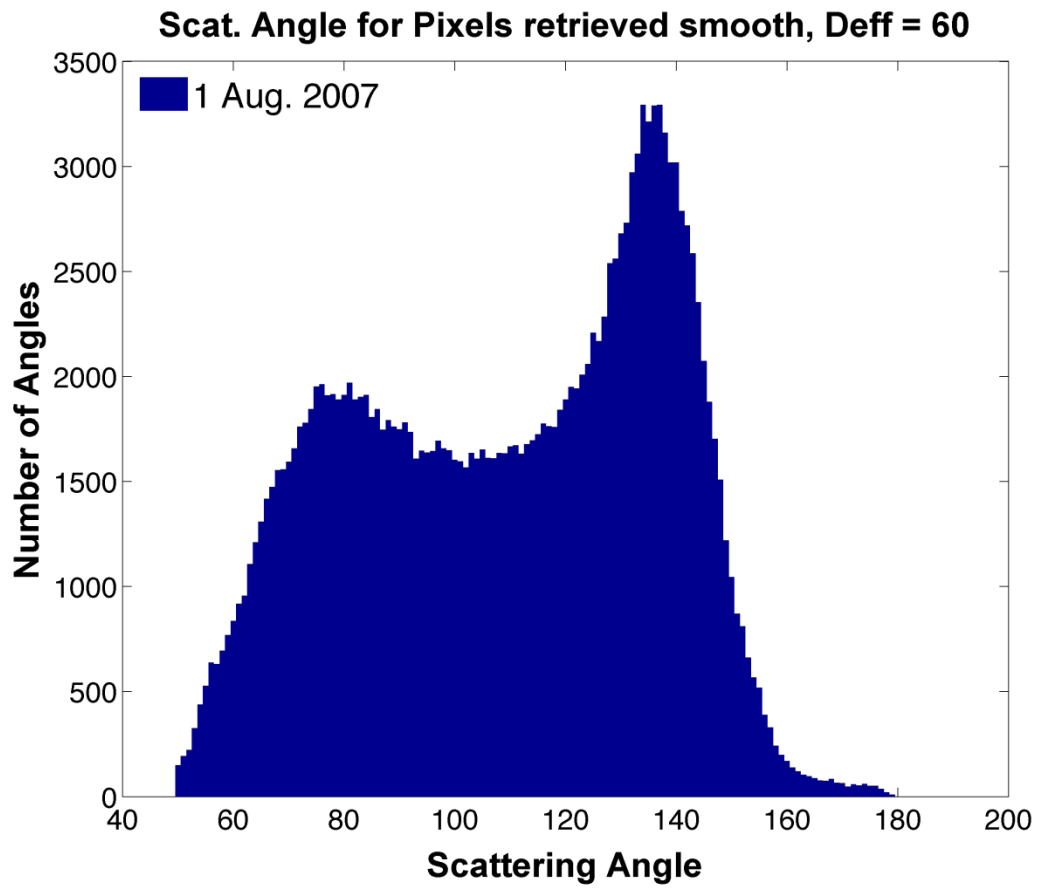
Fig. 35. Histogram of scattering angles for pixels retrieved as smooth. The effective diameter is 60 μm and the PARASOL data is from 1 August 2007. Smooth is a σ value of 0.